Shear wave velocity structure beneath Northeast China from joint inversion of receiver functions and Rayleigh wave group velocities: Implications for intraplate volcanism

Zheng Tang[1], Jordi Julià[2], P. Martin Mai[3], Walter D. Mooney[4], and Yanqiang Wu[5]

[1]The First Monitoring and Application Center, China Earthquake Administration
[2]Universidade Federal de Rio Grande do Norte
[3]King Abdullah University of Science & Technology
[4]United States Geological Survey
[5]The First Monitoring and Application Center, CEA

November 24, 2022

Abstract

A high-resolution 3-D crustal and upper-mantle shear-wave velocity model of Northeast China is established by joint inversion of receiver functions and Rayleigh wave group velocities. The teleseismic data for obtaining receiver functions are collected from 107 CEA permanent sites and 118 NECESSArray portable stations. Rayleigh wave dispersion measurements are extracted from an independent tomographic study. Our model exhibits unprecedented detail in S-velocity structure. Particularly, we discover a low S-velocity belt at 7.5-12.5 km depth covering entire Northeast China (except the Songliao basin), which is attributed to a combination of anomalous temperature, partial melts and fluid-filled faults related to Cenozoic volcanism. Localized crustal fast S-velocity anomaly under the Songliao basin is imaged and interpreted as late-Mesozoic mafic intrusions. In the upper mantle, our model confirms the presence of low velocity zones below the Changbai mountains and Lesser Xing'an mountain range, which agree with models invoking sub-lithospheric mantle upwellings. We observe a positive S-velocity anomaly at 50-90 km depth under the Songliao basin, which may represent a depleted and more refractory lithosphere inducing the absence of Cenozoic volcanism. Additionally, the average lithosphere-asthenosphere boundary depth increases from 50-70 km under the Changbai mountains to 100 km below the Songliao basin, and exceeds 125 km beneath the Greater Xing'an mountain range in the west. Furthermore, compared with other Precambrian lithospheres, Northeast China likely has a rather warm crust (~480-970 °C) and a slightly warm uppermost mantle (~1200 °C), probably associated with active volcanism. The Songliao basin possesses a moderately warm uppermost mantle (~1080 °C).

Shear wave velocity structure beneath Northeast China from joint inversion of receiver functions and Rayleigh wave group velocities: Implications for intraplate volcanism

*Zheng Tang[1,] *, Jordi Julià[2], P. Martin Mai[3], Walter D. Mooney[4], and Yanqiang Wu[1]*

[1]The First Monitoring and Application Center, China Earthquake Administration, Tianjin, China

[2]Departamento de Geofisica, Universidade Federal do Rio Grando do Norte, Natal, Brazil

[3]Earth Science and Engineering Program, King Abdullah University of Science and Technology, Thuwal, Saudi Arabia

[4]Earthquake Science Center, United States Geological Survey, Menlo Park, California, United States

Key Points

- A low S-velocity belt related to Cenozoic volcanism and fast S-velocity anomalies interpreted as mafic intrusions are observed in the crust.
- A high S-velocity anomaly may infer a depleted and refractory lithosphere, inducing the absence of Cenozoic volcanism in the Songliao basin.
- The lithosphere is 50-70 km thick below the Changbai mountains and thickens westward to >125 km beneath the Greater Xing'an mountain range.

Abstract

A high-resolution 3-D crustal and upper-mantle shear-wave velocity model of Northeast China is established by joint inversion of receiver functions and Rayleigh wave group velocities. The teleseismic data for obtaining receiver functions are collected from 107 CEA permanent sites and 118 NECESSArray portable stations.

Rayleigh wave dispersion measurements are extracted from an independent tomographic study. Our model exhibits unprecedented detail in S-velocity structure. Particularly, we discover a low S-velocity belt at 7.5-12.5 km depth covering entire Northeast China (except the Songliao basin), which is attributed to a combination of anomalous temperature, partial melts and fluid-filled faults related to Cenozoic volcanism. Localized crustal fast S-velocity anomaly under the Songliao basin is imaged and interpreted as late-Mesozoic mafic intrusions. In the upper mantle, our model confirms the presence of low velocity zones below the Changbai mountains and Lesser Xing'an mountain range, which agree with models invoking sub-lithospheric mantle upwellings. We observe a positive S-velocity anomaly at 50-90 km depth under the Songliao basin, which may represent a depleted and more refractory lithosphere inducing the absence of Cenozoic volcanism. Additionally, the average lithosphere-asthenosphere boundary depth increases from 50-70 km under the Changbai mountains to 100 km below the Songliao basin, and exceeds 125 km beneath the Greater Xing'an mountain range in the west. Furthermore, compared with other Precambrian lithospheres, Northeast China likely has a rather warm crust (~480-970 °C) and a slightly warm uppermost mantle (~1200 °C), probably associated with active volcanism. The Songliao basin possesses a moderately warm uppermost mantle (~1080 °C).

Plain Language Summary

Northeast China is a unique region with a combination of ancient Precambrian geology and active seismicity and volcanism. The presence of widely distributed volcanoes in this region is enigmatic and their origin has been widely debated. We use available seismic data to create a high-resolution 3-D S-wave seismic velocity model for the crust and upper mantle of Northeast China. Our model reveals significant multi-scale low and high velocity anomalies in the crust, mantle lithosphere and asthenosphere that we associate with the volcanic/magmatic processes. The lithospheric thickness gradually increases from 50-70 km beneath the Changbai mountains to >125 km some 1,000 km to the west. Our results provide novel constraints on the crustal and upper-mantle structure of Northeast China and help to interpret the mechanism behind volcanism and the geodynamics.

Keywords: receiver function, joint inversion, shear-wave velocity, intraplate volcanism, Songliao basin, Northeast China

1. Introduction

Northeast China (Figure 1a) is situated along the eastern margin of the Xingmeng Orogenic Belt, which is surrounded by the Siberian craton to the north, the North China craton to the south, and the subducting Pacific plate to the east (Şengör et al., 1993). This region was formed by the amalgamation of a series of accretionary wedges and micro-blocks (Ge & Ma, 2007; Zhou & Wilde, 2013). Since the late Mesozoic, the Pacific slab westward subduction has played a major role in the tectonic setting and evolution of Northeast China (Deng et al., 1996; Wu et al., 2003). Intensive extensional deformation, along with extensive intraplate volcanism (Wu et al., 2005; Zhang et al., 2010) and development of rift basins (Meng, 2003; Wei et al., 2010), occurred in the area, possibly triggered by the rollback of the Paleo-Pacific slab during the late Jurassic to early Cretaceous (Wang et al., 2006; Wu et al., 2005).

Volcanism in Northeast China has been continuously active during the Cenozoic. Volcanic rocks are spatially distributed along the three belts making up Northeast China: the Changbai mountains (CBM), the Lesser Xing'an mountain range

(LXM), and the Greater Xing'an mountain range (GXM), which bound the Songliao basin (SLB) in the center (Fan & Hooper, 1991; Liu, 1987; Liu et al., 2001). Among hundreds of Cenozoic volcanoes, prominent ones include Changbaishan and Jingpohu volcanoes in the east, Wudalianchi volcano in the north, and Halaha and Abaga volcanoes in the western inland (Figure 1a).

One popular geodynamic model proposes, based on mantle tomography, that Cenozoic volcanism in Northeast China is induced by the stagnation and deep dehydration of the subducted Pacific plate in the mantle transition zone (Ma et al., 2018; Tian et al., 2016; Wei et al., 2012, 2015, 2019; Zhao et al., 2004, 2009, 2012). The Pacific westward subduction and stagnation in the mantle transition zone may have resulted in a big mantle wedge above the subducted slab (Zhao et al., 2009, 2012). The stagnant slab in the mantle transition zone would then continuously release fluids to the big mantle wedge, leading to hot and wet mantle upwellings under Northeast China (Ohtani et al., 2004; Zhao & Ohtani, 2009; Zhao et al., 2009). However, the spatial distribution of the volcanism – volcanoes in the western interior are at least hundreds of kilometers away from those in the east, while the SLB in the center manifests an absence of Cenozoic volcanism – make it difficult to believe that all the volcanoes in Northeast China followed the same formation mechanism (i.e., hot mantle upwelling across a big mantle wedge). Although Cenozoic volcanic activity within a given subregion might have a common origin or be associated with other subregions at deep mantle levels, it seems more likely that each have their own characteristics and geodynamic histories.

Another model suggests that, although still related to deep subduction processes, volcanism in the CBM region is driven by an upwelling of sub-slab mantle materials through a gap in the stagnant Pacific slab (Tang et al., 2014). Both the joint inversion of Rayleigh wave phase velocity dispersion and S-wave travel times (Guo et al., 2018) and the full waveform mantle tomography carried out by Tao et al. (2018) resolve a cylindrical slow velocity anomaly through the mantle transition zone roughly below the CBM region, which is consistent with the above hypothesis above (i.e., mantle upwelling through a slab gap). Additionally, the surface wave tomography of Guo et al. (2016) suggested a mantle convection model in which the mantle upwelling beneath the CBM would induce a downwelling return flow under the SLB. This downwelling would in turn trigger local mantle upwellings below the Halaha and Abaga volcanoes in the west. Although this “mantle upwelling through a slab gap and associated mantle convection” model suggests potential correlations and differences in formation mechanisms among the volcanoes, it does not account for the presence of the Wudalianchi volcano in the northern region. Thus, this model requires additional constraints before it can be become a viable geodynamic model for Northeast China.

Previous studies have investigated the deep crustal and mantle structure of Northeast China. Large-scale body wave travel-time tomography (e.g., Huang & Zhao, 2006; Lei & Zhao, 2005; Li & Van der Hilst, 2010; Ma et al., 2018; Tang et al., 2014; Wei et al., 2012, 2015; Zhang, Wu, & Li, 2013; Zhao et al., 2009; Zhao & Tian, 2013) reported a significant upper-mantle low velocity anomaly down to ~400 km depth below the CBM, a broad high velocity zone that is likely associated with the subducted Pacific slab at the mantle transition zone depths, and possible low velocity anomalies in the asthenospheric mantle roughly beneath the Halaha and Abaga volcanic fields. As mentioned above, Tang et al. (2014) imaged a debated feature: a cylindrical low velocity anomaly rising through the mantle transition zone under the CBM region. Surface wave tomography (e.g., Fan et al., 2020, 2021; Guo et al., 2016; Li et al., 2012, 2013; Pan et al., 2014, 2015) found a low velocity feature at lower-crustal depths under the CBM, upper-mantle low S-velocities and extremely thin lithosphere beneath the CBM, LXM and Sanjiang basin. Receiver function studies (e.g., He et al., 2013; Liu & Niu, 2011; Tao et al., 2014; Zhang et al., 2014; Zhang, Wu, Pan, et al., 2013) constrained crustal thicknesses and bulk Vp/Vs ratios across Northeast China, with crustal thicknesses ranging between 26 and 42 km while bulk Vp/Vs ratios varied between 1.60 and 1.88 (He et al., 2013; Tao et al., 2014). Tao et al. (2014) highlighted isostatic anomalies in the eastern margin of the SLB, the CBM, and the southern GXM. Guo et al. (2015) exhibited high S-velocities in the crust below the SLB. Local geophysical imaging (e.g., Hammond et al., 2019; Gao et al., 2020; Li et al., 2016; Tang et al., 2001; Zhan et al., 2006; Zhang et al., 2002) showed low-velocity and low-resistivity bodies underneath the Wudalianchi and Changbaishan volcanoes, inferring possible crustal magma chambers or partial melts.

Although these studies provide robust geophysical constraints in interpreting the mechanism of intraplate volcanism and the tectonic evolution of Northeast China, important details in structure, particularly fine shear-wave velocity variations at crustal and lithospheric mantle levels, remain ambiguous. Large-scale body-wave travel-time and surface wave tomography studies do not resolve lithospheric details due to the very nature of the datasets. Previous investigations with receiver functions are limited by sparse distribution of stations. Imaging these detailed structures in the crust and lithospheric mantle is thus essential for understanding the correlations and differences among the volcanoes of Northeast China and correctly interpreting their emplacement mechanisms.

In this study, we develop a high-resolution 3-D shear-wave velocity model for

Northeast China using data from a dense seismic experiment. We take advantage of constraints from both receiver functions and surface wave dispersion velocities, which are sensitive to relative variations in velocity structure and absolute background velocities, respectively. A joint inversion of receiver functions and fundamental-mode Rayleigh wave group velocities was performed at each station, so our results map multi-scale S-velocity anomalies and provide novel constraints on the crustal and uppermost-mantle structure. These constraints help in turn to interpret the mechanism behind intraplate volcanism and the geodynamics of Northeast China.

2. Seismic Data

The datasets utilized in this study were assembled from a total of 225 broadband stations in Northeast China (Figure 1b). Up to 107 of these stations were part of the permanent China Digital Seismic Network (ChinaNetwork, 2006) and were operated by the China Earthquake Administration (CEA), while the other 118 sites belonged to the Northeast China Extended Seismic Station Array (NECESSArray), deployed from September 2009 to August 2011. The temporary network NECESSArray improves the spatial station coverage south of ~48°N, where the station distribution is more even and inter-station distances remain less than 70 km. For the 107 CEA sites, over 700 teleseismic events, with epicentral distances between 30° and 90° and body-wave magnitudes above 5.5 within a four-year period (2016-2019) were selected to compute receiver functions (Figure S1a). For the 118 NECESSArray stations, more than 600 events within the same distance range and magnitude threshold between September 2009 and August 2011 were collected (Figure S1b). Note that the selected time windows for each network do not overlap; nonetheless, the spatial distribution of earthquakes recorded by each network is quite similar, with concentration of epicenters along the Mediterranean-Iran-Himalaya belt, the circum-Indian belt, and the circum-Pacific belt (e.g., Mariana and Aleutian Islands).

2.1. Receiver Functions

Receiver functions are time series that carry information about the seismic velocity structure underlying the recording station (Langston, 1979). The time series can be regarded as source-equalized seismic waveforms composed of the direct P wave and secondary phases triggered by the interaction of an incoming P wavefront with near-station subsurface discontinuities. For each discontinuity, the secondary arrivals mainly comprise a P-to-S conversion upon refraction across the interface (Ps) and two multiples reverberating between the free surface and the discontinuity (PpPs and PpSs + PsPs). The seismic velocity variations with depth below the recording station can be determined by modeling the relative travel-times and amplitudes making up the receiver function waveforms (Ammon et al., 1990; Owens et al., 1984).

Receiver functions are estimated by deconvolving the vertical component of teleseismic P wave recordings from the corresponding horizontal components. For that purpose, we applied a time domain iterative deconvolution technique (Ligorría & Ammon 1999) with 500 iterations. Before deconvolution, we windowed the three-component seismograms 10 s prior to the P wave arrival and 110 s after, demeaned, detrended, tapered and band-pass filtered the traces between 0.05 and 4 Hz to prevent low- and high-frequency noise and aliasing. Subsequently, we down-sampled the filtered waveforms to 10 samples per second and rotated the horizontal components around the vertical component into the great-circle path to determine the corresponding radial and transverse traces. Finally, both radial and transverse receiver functions were obtained by deconvolving the vertical component from the radial and transverse components, respectively. Although the transverse receiver functions were not included during the analysis, they help to assess lateral heterogeneities and anisotropy of the subsurface (Savage, 1998). In addition, we employed a Gaussian low-pass filter to limit the frequency content of the deconvolved traces. For each event, receiver functions in both the high (fc $\leq$ 1.25 Hz, Gaussian width α = 2.5) and low (fc $\leq$ 0.50 Hz, Gaussian width α = 1.0) frequency bands were obtained for the subsequent joint inversion, as they contain information on velocity heterogeneities at different scales and help to distinguish velocity jumps from gradational transitions (Julià, 2007).

Following Tang et al. (2016, 2019), a two-step quality control was employed to retain high-quality receiver functions. First, receiver functions that did not reproduce at least 85% of the horizontal traces when convolved back with the corresponding vertical seismograms were rejected. Second, we visually examined transverse receiver function waveforms and those with abnormally large amplitudes in the transverse component were disregarded. As mentioned above, large transverse amplitudes may result from lateral heterogeneities and/or anisotropy (Savage, 1998) but may also indicate failure during rotation into the great circle path. Unstable and extremely distorted radial receiver functions were also visually removed from the dataset. Overall, from the permanent CEA network, a total of 16,848 radial receiver functions in the high-frequency band (fc $\leq$ 1.25 Hz) and 16,096 radial receiver functions in the low-frequency range (fc $\leq$ 0.50 Hz) were kept from the initial selection of 63,838 seismograms. Additionally, 12,135 radial receiver functions at Gaussian width of α = 2.5 and 11,796 receiver functions at Gaussian parameter of α = 1.0 from the temporary NECESSArray stations were accepted after our quality control, out of a total of 59,919 teleseismic waveforms.

Receiver function waveforms recorded by some stations in sedimentary basins are sometimes dominated by high-amplitude, low-frequency ringy signals that result from seismic energy reverberating in the low-velocity sedimentary layer. The reverberations may partially or totally mask the P-to-S conversions generated at deep seismic interfaces, making it difficult to extract structural information from deep crustal or upper-mantle levels (e.g., Julià et al., 2004; Zelt & Ellis, 1999). We therefore applied a resonance removal filter (Yu et al., 2015) on those receiver functions to effectively eliminate or significantly reduce the multiples associated with low-velocity sediments, but keeping the primary P-to-S conversion generated at the sediment-bedrock interface. The basic idea is to apply a frequency-domain filter of the form $(1 + r_0 e^{-i\omega\Delta t})$ to the original receiver function, where the strength of the near-surface reverberations (r_0) and the two-way traveltime (Δt) for the reverberations are determined from the normalized autocorrelation function. An example performing the resonance removal filter with real data recorded by station NEA7 is shown in Figure S2. Note that the original receiver functions in both frequency bands (Figure S2a, b) at NEA7 are ringy. After the resonance removal filter, the ringing components of the signal are effectively reduced in the deconvolved traces (Figure S2c, d). Additionally, a synthetic test (Figures S3-S5) demonstrates that the resonance removal filter effectively removes the multiples of converted shear waves within sedimentary layer and successfully recovers the desired P-to-S signals generated at deep discontinuities in both lag time and amplitude.

Subsequently, for each station and Gaussian width, we grouped receiver functions from similar directions (i.e., back-azimuth) and comparable epicentral distances (i.e., ray-parameter) into bins to then average them. Within each bin, we constrained the maximum deviations in ray-parameter and back-azimuth to no more than 0.01 s/km and 10°, respectively. Every bin was composed of at least 3 deconvolved traces. Therefore, several receiver function averages with different average back-azimuths and ray-parameters were obtained for each station, sampling the Earth in various directions at each recording site to reflect the effects of azimuthal variations. Figure 2 exhibits selected radial receiver function averages at both Gaussian widths for a few stations. Generally, the time series reveal clear Ps conversions and reverberations due to the Moho discontinuity. At some sites (e.g., NE38, NE68, NE78, NEA6, NEA7, and NEAB), the receiver function averages are the result of applying the resonance removal filter mentioned above.

2.2. Rayleigh Wave Group Velocities

An independent tomographic study carried by Li et al. (2013) provided local Rayleigh wave group velocities for each station. Li et al. (2013) measured fundamental-mode Rayleigh wave group velocities from earthquakes that are mostly located on the circum-Pacific belt, the circum-Indian belt and western China. They compiled observations from permanent stations operated by CEA in mainland China and temporary arrays (e.g., GEOSCOPE, KNET, and KZNET) deployed in adjacent areas. They performed single-station measurements of group velocity applying a wavelet transformation frequency-time analysis method (Wu et al., 2009). Rayleigh wave dispersion curves were acquired at periods between 10 and 145 s along more than 9,500 paths across the entire East Asia region. Subsequently, Rayleigh wave group velocities were tomographically inverted on a 2-D rectangular grid with node spacing of 1° in both latitude and longitude. The best resolution of their 2-D group velocity maps for the majority of East Asia is roughly 3° according to checkerboard tests (Li et al., 2013).

3. Joint Inversion

Receiver functions are usually inverted for shear wave velocity structure, although they are also theoretically sensitive to compressional wave velocities and densities (Owens et al., 1984). Previous studies illustrated that the main sensitivity of receiver function is to relative velocity contrasts and vertical S-P travel-times, not to absolute vertical S-velocities (Ammon et al., 1990). Thus, receiver functions can resolve small-scale relative shear-wave velocities, but the inverse problem is non-unique. Surface wave dispersion curves, in contrast, constrain averages of absolute S-velocities within frequency-dependent depth-ranges, although the wavelengths associated with surface waves cannot resolve small-scale variations (Julià et al., 2000). Therefore, we take advantage of the complementarity of receiver functions and surface wave dispersions to jointly invert both datasets, so that the inverted models reflect average background velocities constrained by the dispersion data with the details from the receiver function dataset superimposed. Moreover, the non-uniqueness of receiver function inversion is significantly reduced with the addition of surface wave dispersion measurements (Julià et al., 2000).

3.1. Joint Inversion Details

Applying the linearized scheme of Julià et al. (2000, 2003), we conducted the joint inversion of receiver functions and Rayleigh wave group velocities to obtain a shear-wave velocity-depth profile of the crust and upper mantle at each station. Conceptually, the joint inversion summarizes the structural information contained in both receiver function and dispersion curve into a simplified 1-D Earth model. To equalize the contributions from each dataset, both sets of observations are normalized by the number of data points and the corresponding physical units (Julià et al., 2000). Also, an *a priori* factor that controls the relative influence of each dataset into the joint inversion is employed. We chose 0.5 for this parameter to give equal weight to each dataset in our calculations. In addition, the inversion employs a depth-dependent smoothing on the velocity-depth profiles, which allows rapid perturbations of shear-wave speed at shallow layers (i.e., 0–55 km depths) but suppresses large velocity variations at deep levels (i.e., below 55 km depth). The smoothness constraint consists of minimizing the second velocity differences among adjacent model layers. A smoothness factor, which controls the trade-off between model smoothness and matching the observations, was set to be 0.2 after trial and error.

The model is parameterized in terms of homogeneous horizontal layers with fixed thickness and velocity. Layer thicknesses are 2.5 km at depths of 0–60 km, 5 km at 60–150 km, and 10 km under 150 km depth (maximum depth considered: 400 km). The P-wave velocity is estimated by assuming a constant Vp/Vs ratio (1.75 for 0-40 km depths; 1.81–1.85 for 40-km-depth below) for each layer. Density is inferred from the resulting compressional velocity through the empirical relation of Berteussen (1977). The initial model needed for the linearized joint inversion comprises a 40 km thick crust with gradually increasing S-velocities from 3.4 to 4.0 km/s and a flattened PREM (Preliminary reference Earth model) upper mantle (Dziewonski & Anderson, 1981).

Sedimentary structure generally leads to complex receiver function waveforms, despite a resonance removal filter being applied to eliminate or suppress the near-surface reverberations. For stations situated on sediments, we found it necessary to guide the joint inversion through the inclusion of a near-surface layer with slow (sediment like) velocities in the starting model. For those stations, we tested different thickness of the near-surface layer (i.e., 1.0, 1.5, 2.0, and 2.5 km) and used a sedimentary shear-wave velocity of 1.71 km/s in all cases. Also, a stronger smoothness constraint (i.e., 0.5) was required to prevent numerical instabilities during the inversion process.

We inverted for S-wave velocities only above 270 km depth, although the model was parameterized down to the bottom of the upper mantle (400 km depth). The approach of Julià et al. (2000, 2003) allows fixing the S-wave velocities of given layers to predetermined values by applying an extremely high weight for those layers. For the deep levels below 270 km depth, shear velocities were forced to be PREM-like during the inversion, thus accounting for the partial sensitivity of long-period dispersion velocity to deep Earth structure (Julià et al., 2003, 2009).

3.2. Shear Wave Velocity Profiles and Uncertainties

We obtained shear-wave velocity-depth profiles at 225 stations by jointly inverting the receiver functions with local Rayleigh wave group velocities. Figure 3 presents the joint inversion for the permanent station WDL situated on the LXM (the location is marked in Figure 2). For this case, a total of 13 receiver function averages, which sample the subsurface from various directions (i.e., average back-azimuths between 43° and 310°) and different incident angles (i.e., average ray-parameters of 0.044-0.077 s/km), were computed in both the high- and low-frequency bands. All average waveforms, particularly the prominent Ps conversion and two multiples from the Moho discontinuity, are consistently observed at similar lag times. This indicates that the Earth structure underlying the station can be successfully modelled through a single 1-D velocity-depth profile, although some small-scale azimuthal variations may exist. Both the predicted receiver function and dispersion data match the corresponding observations very well. The resulting 1-D model shows a 30 km thick crust consisting of an upper crust with S velocities of 3.3–3.4 km/s down to 12.5 km and a lower crust with shear velocities of 3.5–3.7 km/s at 12.5–30 km depth. The Moho interface is sharp and located at 30 km depth. In the upper mantle, a low velocity anomaly with shear-wave speeds of 4.2–4.3 km/s between 40 and 60 km depth and a low velocity zone starting roughly at 100 km depth are imaged.

Another example is displayed in Figure 4 for the temporary station NE4A in the CBM region (the location is shown in Figure 2). A total of 11 receiver function groups were formed, with ray-parameters between 0.045 and 0.075 s/km and back-azimuths in the 55°-230° range. As before, an average 1-D velocity-depth profile was inverted from all receiver function averages and dispersion velocities. The model reveals a sharp Moho at 32.5 km depth. Above the Moho, the crust consists of a 12.5 km thick upper crust with a possible low velocity zone at 7.5–12.5 km depth, a middle crust with gradually increasing S-wave velocities from ~3.6 to ~3.8 km/s between 12.5 and 27.5 km depth, and a fast-velocity lower crust with shear velocities of 3.9–4.1 km/s at 27.5–32.5 km depths. The upper mantle contains a very thin lid of ~7.5 km followed by slow velocities down below. Particularly, below ~85 km depth, S-wave velocities slower than 4.25 km/s are revealed.

As mentioned in section 3.1, for a few sites that overlie sediments, we performed several joint inversions in order to test different sedimentary layer thicknesses and obtain a solution that best matched the receiver function waveforms. To that effect, we divided the top 2.5-km of the general starting model into two layers: an uppermost layer with a sediment-like S-wave velocity of 1.71 km/s, and a lowermost layer with a more crystalline-basement velocity of 3.42 km/s. The thickness of the sediment was set to 1.0, 1.5, 2.0, and 2.5 km, successively. An example for station NEA6 (in the SLB, see Figure 2) illustrating the above procedure is provided in the supplementary document (Figures S6–S10). Without considering sedimentary structures, the joint inversion would simply not converge to a stable solution (Figure S6); even for a 1.0 km thick sedimentary layer in the starting model, the solution was still not converging (Figure S7). Assuming a thicker sedimentary layer (i.e., 1.5, 2.0, and 2.5 km), the inversions yielded more stable solutions (Figures S8–S10). Furthermore, the match between predicted and observed data, particularly for the P-to-S conversions between 1 and 4 s (likely corresponding to sedimentary structure) in receiver functions and the Rayleigh wave dispersions at shorter periods, was superior when we considered a 1.5 km thick sedimentary layer (Figures S8-S10). Accordingly, we regarded this inverted S-wave velocity profile (Figure S8) as the final solution for station NEA6.

Small misfits in the receiver function waveforms (Figures 3, 4) remain nonetheless after modelling all the averages and dispersion curve with a single velocity-depth profile. These small discrepancies, probably indicative of localized lateral variations in Earth structure, allow us to assess the uncertainties of 1-D inverted shear-wave velocity models (e.g., Julià et al., 2009). At a given station, we achieved single-group S-wave velocity models by jointly inverting the dispersion curve with each individual receiver function average (both high- and low-frequency). The standard deviations of these single-group models were considered as the approximate uncertainties (i.e., confidence bounds) for the average velocity model. The above steps were carried for all stations and the uncertainties were displayed around the average 1-D velocity-depth profiles (Figures 3, 4). Note that the accuracy of the confidence bounds is affected by the number of receiver function groups and the regularization parameters for each station. Nevertheless, we think this approach successfully conveys the degree of lateral variation around the station and provides a good approximation of the range of variation in S-velocity.

4. Crustal and Upper-Mantle Structure of Northeast China

With the 225 irregularly distributed 1-D velocity profiles, we generated a 3-D shear-wave velocity model of the crust and upper mantle in Northeast China by applying a bilinear interpolation for each depth layer. For those stations where we imposed a thin, near-surface layer to model sedimentary structure, the Voigt average of the top 2.5-km was calculated to ensure a consistent format. In this section, we present horizontal and vertical slices of our final 3-D model across the entire study area.

4.1. Horizontal slices of Shear-Wave Velocity

Figures 5-7 display a series of horizontal absolute S-velocity maps at different depths. At shallow levels (i.e., 0–5.0 km, Figure 5a, b), the velocity patterns are dominated by the presence or absence of sediments. The slow velocities correlate well with the thick sedimentary cover of the SLB, Sanjiang, Hailar and Erlian basins, consistent with previous investigations (e.g., Feng et al., 2010; Liu et al., 2016; Guo et al., 2016). Particularly, the border outlining the low velocities in the center of the study area closely coincides with the geological boundary of the SLB. At 7.5-15 km depth (Figure 5d-f), the velocity distributions appear reversed with respect to the shallower maps. The SLB is characterized by S-wave velocities that are faster (~3.6-3.9 km/s) than the surrounding areas (~3.2-3.6 km/s). Between 15 km and 25 km depth (Figure 5g, h, and Figure 6a, b), the shear-wave velocities fluctuate around a mean crustal velocity of ~3.6 km/s, although moderately slow velocities are imaged below the LXM (around the Wudalianchi volcano) and the northern margin of the North China craton.

At crust-to-mantle transition levels (i.e., 27.5–37.5 km, Figure 6d-g), a fast/slow S-velocity split across the GXM is imaged. As shown later, this pattern results from changes in crustal thickness, so that velocities West and East of the GXM correspond to mapping the lower crust and uppermost mantle beneath the region, respectively. At 37.5-40 km (Figure 6h), most of the study area displays shear velocities higher than 4.3 km/s - except some local regions in the West at roughly 117°E longitude - demonstrating that upper mantle levels have been reached beneath Northeast China.

At shallow mantle levels (i.e., 40-65 km, Figure 6i–l, and Figure 7a-c), the reversed velocity pattern imaged at upper-crustal depths (i.e., 7.5-15 km, Figure 5d-f) seems to reappear. The SLB in the center exhibits high-to-moderate S-velocities, while low velocities mainly concentrate on the surrounding areas. In the deeper mantle (i.e., 70-125 km, Figure 7d-i), a reversed fast/slow S-velocity split pattern is revealed. At 70-75 km depth, the east (i.e., the CBM, Sanjing basin) is characterized by lower S-velocities, while the west shows high velocities. As depth increases, low velocity zones expand westward.

4.2. Map of Crustal Thickness

To illuminate the contrast in crustal thickness across the entire study area, we constructed a map of crustal thickness based on the inverted S-velocity models. Velocities above 4.2 km/s are interpreted as indicative of (hot) uppermost mantle lithologies. With this simple criterion, we first extracted a crustal thickness estimate below each station and then constructed a 2-D map through a bilinear interpolation.

Figure 8 compares the resulting map of crustal thickness with that from the global reference model CRUST1.0 (Laske et al., 2013). In general, the two maps exhibit similarities in large-scale features such as a relatively thicker crust in the west (i.e., the GXM and its western flank) and a thinner crust in the east (including the CBM, LXM, SLB, and Sanjiang basin). However, our high-resolution results indicate several detailed features that differ significantly from the reference model. For example, our model reports a thinner crust of ~30 km in the easternmost portions of the SLB and LXM, although the locations of minimum crustal thickness for each map coincide. Additionally, our results reveal a thick crust of more than 40 km west of ~117°E, but not under the GXM as inferred by CRUST1.0.

The most intriguing feature resolved by our model, however, is the abrupt change in crustal thickness between the Songliao block and Jiamusi massif on either side of the Mudanjiang fault. Previous studies (Oh, 2006; Wu et al., 2011) claimed that the Jiamusi massif is possibly an exotic terrane from the Yangtze plate or the Gondwanan crust. Zhou & Wilde (2013) proposed the Jiamusi massif split away at ~230 Ma, and subsequently re-docked with the Songliao block between 210 and 180 Ma. Our results demonstrate the difference in crustal thickness between the two blocks.

4.3. Vertical Slices of Shear-Wave Velocity

Vertical sections of S-velocity are plotted in Figures 9-11 for crustal levels (0-50 km), and in Figures 12-14 for upper-mantle levels (25-125 km). Profiles A1 to A4 are oriented in a west-east direction along latitudes of 48°N, 46°N, 44°N, and 42°N, respectively. Cross sections B1 to B3 are along longitudes of 120°E, 124°E, and 128°E in a south-north orientation. Transects C1 to C3 are trending NW-SE.

The vertical slices reveal detailed structural information at crustal and upper-mantle depths. In the crust, we observe four main features: (1) a low shear velocity belt at 7.5-12.5 km depth below Northeast China except the SLB (Figures 9-11), (2) a very fast S-velocity body at 8-30 km depth under the SLB (see sections A1, A2, A3 in Figure 9, B2 in Figure 10, and C2 in Figure 11), (3) high S-velocities between 15 and 35 km depth beneath the CBM region (see profiles A2, A3, A4 in Figure 9, B3 in Figure 10, and C1, C2 in Figure 11), and (4) some high velocity anomalies at 10-25 km in the west (profiles A2, A3 in Figure 9, and C3 in Figure 11).

In the upper mantle, the most intriguing features are the multi-scale, low shear-wave velocity anomalies below the CBM (see cross sections A3, A4 in Figure 12, B3 in Figure 13, and C2 in Figure 14) and LXM (see A1 in Figure 12, B3 in Figure 13, and C1 in Figure 14). An additional low velocity zone at 40-60 km depth is revealed beneath the LXM. A few small-scale low S-velocity anomalies are also imaged at shallow levels (i.e., 40-60 km, Figures 12-14), implying a more complex system in Northeast China. In addition, a remarkable high velocity anomaly under the SLB at roughly 50-90 km depth (see profiles A2 in Figure 12, B2 in Figure 13, and C2 in Figure 14) is observed.

A decrease in shear-wave velocity below 4.3 km/s is interpreted as representative of the lithosphere-asthenosphere boundary (LAB). Our model infers a very thin lithosphere of 50-70 km thick under the CBM, and a lithospheric thickening westward (A3, A4 in Figure 12, and C2, C3 in Figure 14). Both the SLB and LXM have a roughly 100 km thick lithosphere (A1, A3 in Figure 12, B3 in Figure 13, and C1, C2 in Figure 14). The lithospheric thickness under the SLB in our model disagrees with the recent surface wave tomography of Guo et al. (2016) (they reported high S-velocities at 50-200 km depths below the SLB), but is consistent with the previous geophysical studies (e.g., Li et al., 2012; Zhang et al., 2014). Furthermore, we do not observe the LAB within our depth-range (i.e., 0-125 km) beneath the GXM and its western flank. This suggests a thicker lithosphere, in agreement with previous studies (e.g., Zhang et al., 2014).

5. Discussion and Implications

The most prominent signatures from our 3-D model are the multi-scale shear-wave velocity anomalies at different depths in the study area. In the following, we first discuss possible factors that may be responsible for the observed S-velocity anomalies in the crust and upper mantle. Then, we compare the lithospheric S-velocity structure of Northeast China and the SLB with the Precambrian lithospheres of the Arabian shield and North American craton as well as the lithosphere of the Basin and Range in Western United States, respectively.

5.1. Crustal Shear Velocity Anomalies

We image a low S-velocity belt at roughly 7.5-12.5 km depth. Interestingly, the belt covers the entire Northeast China region except the SLB in its center (Figure 5d, e). This pattern coincides with the widespread distribution of Cenozoic volcanism in the region, which is absent in the SLB. Thus, the existence of the low S-velocity belt at upper-crustal depths appears to be associated with Cenozoic volcanism/magmatism in Northeast China.

Several factors could be involved in the reduction of crustal S-velocity, such as temperature increase, presence of partial melt, and fluid-filled faults (Tang et al., 2019; Wang et al., 2019). Considering that surface heat-flow varies between 40 and 105 mWm^2 in Northeast China (Gosnold, 2011), it seems plausible to assume a warmer-than-average crust for Northeast China. Absolute S-wave velocities within the belt are roughly between 3.2 and 3.4 km/s in our model, so S-velocity reductions are approximately 0.06-0.26 km/s (equivalent to 1.7-7.5%) relative to the AK135 reference model (the upper-crustal shear velocity is 3.46 km/s). A temperature increase in the wide 170-740 °C range may explain the observed velocity reductions through the scaling relationship $\partial V_s/\partial T = 0.35\, ms^{-1}K^{-1}$ (Sumino & Anderson, 1982). Temperatures at 10 km depth are usually within the 120-300 °C range for the given surface heat-flow (Christensen & Mooney, 1995), so such a large temperature increase seems unlikely at this depth. Therefore, although temperature is possibly contributing, it may not be the only cause for the observed upper-crustal low velocity belt.

Ascending magmas may stall within the crust and lead to strong fractional crystallization (Fan et al., 1999, 2005). Local geophysical studies (e.g., Hammond et al., 2019; Gao et al., 2020; Kyong-Song et al., 2016; Li et al., 2016; Tang et al., 2001; Zhang et al., 2002) reported evidence of crustal partial melts and/or magma reservoirs under the Wudalianchi and Changbaishan volcanic fields. Additionally, deep magmas were transported upward through the crust via the development and propagation of faults (Downs et al., 2018). Meanwhile, some liquid and/or gas could have migrated into these faults, changing the physical properties of the nearby rock. Thus, partial melt and fluid-filled faults are also likely significant causes for producing the crustal low S-velocity belt below active magmatic provinces.

Our model resolves three significant crustal high velocity features. The most remarkable one is the extremely fast S-velocity body at 8-30 km below the SLB, which corroborates previous findings (Guo et al., 2015), but is imaged here with improved spatial resolution. The very large S-velocity anomaly in the crust was interpreted as solidified mafic intrusions, consistent with the scenario of widespread volcanism/magmatism in the region, followed by cooling and subsidence during the late Mesozoic under the SLB (Feng et al., 2010).

Beneath the active Cenozoic magmatic province - CBM, high S-velocities at 15-35 km depths are observed in our model. This observation differs from the recent surface wave tomographic study of Fan et al. (2020), in which they reported a slow S-velocity anomaly attributed to a potential lower-crustal magma reservoir below the CBM. We interpret the observed fast S-velocity underneath the CBM as the result of middle to lower-crustal magmatic intrusions (through cooling and solidification).

Like the SLB, the GXM also experienced extensive volcanism/magmatism possibly caused by delamination and consequent asthenospheric mantle upwelling during the late Mesozoic (Wang et al., 2006; Wu et al., 2005; Zhang et al., 2010). Thus, we observe crustal high S-velocity anomalies (at 10-25 km depth) that probably reflect magmatic intrusions, although the size of the fast S-velocity anomalies under the GXM and its western flank is not comparable to that of the one below the SLB. Geochemical studies (e.g., Zhang et al., 2010) reported granite emplacement in Mesozoic volcanic rocks in the GXM. This finding may explain why felsic crust is predominant under this subregion (Guo et al., 2016).

Interestingly, below the LXM (around the Wudalianchi volcano), no fast S-velocity anomaly is observed at crustal depths, which is obviously different from the other active Cenozoic magmatic provinces such as the CBM. The LXM shows a lower crust with moderately slow shear velocities. Recent local investigations (Gao et al., 2020; Li et al., 2016) imaged an extremely low-resistivity and low-velocity body, interpreted as a magma chamber, at upper-crustal levels below one vent of the Wudalianchi volcano. Accordingly, the observed moderately low S-velocity in the lower crust may be associated with upward transportation of magmas and charging of the crustal reservoir from deep mantle sources.

5.2. Upper-Mantle Shear Velocity Anomalies

Our model confirms the existence of a pronounced upper-mantle low shear velocity zone beneath the CBM, which is consistent with previous studies (e.g., Guo et al., 2016; Li et al., 2012; Pan et al., 2015; Tang et al., 2014; Zhao et al., 2009). Our model resolves new details about the low velocity zone including its geometry and minimum absolute velocity. S-wave velocities less than 4.25 km/s can be regarded as representative of partial melts in the upper mantle, particularly beneath volcanically active fields (Plank & Forsyth, 2016). Therefore, the observed low velocity zone (Vs < 4.25 km/s) strongly suggests the presence of partial melts in the upper mantle.

Previous studies proposed hot and wet upwelling flows in a big mantle wedge (Zhao et al., 2004, 2009) or an upward escape of melted sub-slab materials through the stagnant Pacific slab gap in the mantle transition zone (Tang et al., 2014), which triggered the volcanism. While the deep mantle dynamics are still debated, there is widespread agreement that the upwelling of hot sub-lithospheric melts feed the volcanism in the CBM. A mantle anisotropy study of Li et al. (2017) with SKS data reported extensive null splitting in the CBM, likely consistent with the upwelling model. Thus, the imaged upper-mantle low velocity zone most likely reflects a large volume of upwelling mantle melts.

Some studies (e.g., Wei et al., 2019; Zhao et al., 2009) speculated that the Cenozoic volcanism in the LXM (e.g., Wudalianchi volcano) has the same origin as the volcanoes in the CBM: triggered by upward flows of hot mantle materials. Below the LXM, we image a pronounced upper-mantle low velocity zone (Vs < 4.25 km/s, below ~100 km) that can be interpreted as upwelling asthenospheric mantle melt, consistent with the dynamic model of Zhao et al. (2009). However, our results exhibit an additional low S-velocity anomaly in the uppermost mantle (Vs < 4.25 km/s, at 40-60 km depth), probably representing partial melts also beneath the LXM. The distinctions between the LXM and CBM in lithospheric structure include: (1) moderately slow S-velocity under the LXM versus high S-velocity below the CBM in the lower crust, (2) a 30 km thick crust under the LXM versus a roughly 35 km thick crust under the CBM,

(3) a ~100 km thick continental lithosphere containing an uppermost-mantle low S-velocity anomaly at 40-60 km beneath the LXM versus thinner lithosphere (50-70 km) under the CBM, which may be associated with the differences in volcanic/magmatic activity and basalt geochemistry in the two provinces (Fan et al., 2021).

The SLB is the center of the late Mesozoic rifting and lithospheric thinning in eastern China (Ren et al., 2002). Our model displays a thin lithosphere (~100 km) below the SLB, consistent with the episode of the intensive extension (Feng et al., 2010; Ren et al., 2002). However, an interesting phenomenon is the absence of Cenozoic volcanism in the SLB. Invoking the model of wet, hot upwelling caused by dehydration of the stagnant Pacific slab in the mantle transition zone (Zhao et al., 2009, 2012) raises a problem: why did volcanism not occur in the SLB during the Cenozoic, as it did in the western interior (e.g., Halaha and Abaga volcanoes)? One possible explanation is that the extensive volcanic/magmatic activities during the late-Mesozoic depleted the lithosphere under the SLB and made it more refractory. Thus, the lithosphere of the SLB could not produce any melts for Cenozoic volcanism. One evidence - a positive mantle velocity anomaly under the SLB (at 50-90 km depth) revealed by our model can support this hypothesis.

Another possibility is invoking the mantle convection model raised by Guo et al. (2016). They proposed the mantle upwelling below the CBM led to a downwelling asthenospheric flow under the SLB. If the hypothetical mantle convection exists, the hot sub-lithospheric melts beneath the SLB would lack the driving force to migrate upward and would not induce volcanism. Mantle anisotropy studies (Chen et al., 2017; Li et al., 2017) exhibited many nulls in the CBM, a few nulls in the southwestern SLB, and some nearly NW-SE fast polarization directions in between from shear wave splitting measurements. The nulls in the southwestern SLB are attributed to the downwelling limb of the convection cell (Li et al., 2017).

A simple asthenospheric mantle flow usually cannot explain the observed seismic anisotropy, which also reflects historical tectonic deformation preserved in the lithosphere (Li & Niu, 2010; Liu et al., 2016; Qiang & Wu, 2015). In the SLB, weak azimuthal anisotropy approximately corresponding to crustal and lithospheric mantle depths suggests that historical deformation records in the lithosphere were erased by the extensive volcanism/magmatism in the late Mesozoic (Liu et al., 2016). Accordingly, we could consider the asthenospheric mantle flow as the dominant factor determining the mantle anisotropy of the SLB.

However, only a few stations show nulls. Moreover, complicated variations of shear wave splitting within the SLB were observed (Chen et al., 2017; Li et al., 2017). Thus, there is still insufficient evidence to support a downwelling flow in the SLB due to mantle convection. Besides, a high P-wave velocity anomaly resting atop the 410 km discontinuity under the SLB was imaged and interpreted as detached continental lithosphere by Wei et al. (2019). If their imaging and interpretation are correct, the continuous sinking of the delaminated lithosphere could induce an upward flow, in conflict with the mantle convection model.

5.3. Comparison with Other Lithospheric Models

For comparison, we average the 225 1-D shear-wave velocity models obtained from the joint inversion at each station to generate a single 1-D average model for Northeast China. Also, we average all the 1-D S-velocity models from the stations located in the SLB to obtain one average 1-D model that represents the extended lithosphere of the SLB. Figure 16a compares the S-velocity structure of Northeast

China with the Precambrian lithospheres of the Arabian shield (Tang et al., 2019) and the North American craton (Shen & Ritzwoller, 2016). Additionally, Figure 16b exhibits the comparison between the rift lithosphere of the SLB in Northeast China and that of the Basin and Range (Shen & Ritzwoller, 2016) in Western United States.

Generally, the Precambrian crusts of different regions appear similar (Figure 15a). Both the Arabian shield and Northeast China have a thinner crust of ~35 km, compared with the North American craton (~45 km thick crust). That is probably because the former two experienced intensive rifting (Ebinger & Sleep, 1998; Ren et al., 2002). Above all, one significant observation from the 1-D average model of Northeast China is the constant Vs (~3.6 km/s) between 15 and 27.5 km, distinctly different from the Arabian shield and the North American craton. What could be the major factor to induce a near-zero seismic velocity gradient within the depth levels? We attribute it to temperature and conclude that the crust of Northeast China is likely rather warm, although other potential factors such as crustal partial melts within some local areas may also contribute.

The reductions in S-velocity at 15–27.5 km depths below Northeast China are approximately 0.1-0.2 km/s, compared with the Arabian shield and the North American craton. The corresponding crustal temperature increases are 280-570 °C, simply estimated with the relationship $\partial V_s/\partial T = 0.35\ ms^{-1}K^{-1}$(Sumino & Anderson, 1982). Considering the temperature-depth models for Eastern United States (200-400 °C between 15 and 27.5 km for average heat flow, Blackwell, 1971; Christensen & Mooney, 1995), however, temperatures within 15–27.5 km depth in Northeast China are probably larger, around 480-970 °C (consistent with high heat flow).

Furthermore, for Northeast China, the S-velocity of the uppermost mantle is approximately 4.35 km/s, which is ~0.1 km/s lower than the Arabian shield and North American craton. This characteristic probably suggests a slightly warm uppermost mantle. Temperature anomalies at both the crust and uppermost mantle are likely associated with the active intraplate volcanism in Northeast China.

Using the first-order Taylor expansion of the pressure-temperature dependence of the shear wave velocity, $V_s(P,T) = V_0(P_0,T_0) + \frac{\partial V_s}{\partial P}(P - P_0) + \frac{\partial V_s}{\partial T}(T - T_0)$, we simply estimate the average temperature of the uppermost mantle in Northeast China. This expression relates V_s at a given pressure P and temperature T with a reference velocity V_0 at pressure P_0 and temperature T_0 through the partial derivatives $\partial V_s/\partial P$ and $\partial V_s/\partial T$. Assuming that the dominant rock within the uppermost mantle is peridotite, the estimates for the reference velocity $V_0 = 4.72\ km/s$ (at pressure $P_0 = 0\ kbar$ and temperature $T_0 = 0\ °C$) and the partial derivatives ($\partial V_s/\partial P = 0.946 \times 10^{-2}$ km/s·kbar and $\partial V_s/\partial T = -3.93 \times 10^{-4}$ km/s·°C) are taken from Kern & Richter (1981). Pressure is estimated as $P = \sum_i \rho_i\, g h_i$, where is i the layer number, ρ_i represents the density at ith layer from the average 1-D model, g is gravity acceleration, and h_i represents the thickness of ith layer. For the average S-velocity (~4.35 km/s) of the uppermost mantle (at 40 km depth), the estimated temperature is ~1200 °C.

For comparison between the SLB and the Basin and Range (Figure 15b), we note that the SLB has a pronounced fast S-velocity anomaly at 7.5-17.5 km depth, which is interpreted as solidified mafic magmatic intrusions during the late Mesozoic. Additionally, the S-velocity of the uppermost mantle in the Basin and Range is about 4.2 km/s, much lower than that (~4.4 km/s) of the SLB. The Basin and Range has a significantly warm upper mantle (Blackwell, 1971; Christensen & Mooney, 1995). Thus, this implies the Basin and Range is much warmer than the SLB, which is moderately warm. With the same approach introduced above, the estimated average temperature of the uppermost mantle (at 40 km depth) of the SLB is ~1080 °C.

6. Conclusions

We have constructed a high-resolution 3-D S-wave velocity model of the crust and upper mantle for Northeast China by jointly inverting receiver functions and fundamental-mode Rayleigh wave group velocities for 225 broadband seismic stations. Our results reveal the detailed lithospheric and sub-lithospheric structure, and shed light on the volcanic/magmatic processes and dynamics (Figure 16). Our main findings and interpretations associated with the shear velocity structure in Northeast China are shown in Figure 16 and summarized as follows:

1. We observe a low S-velocity belt at 7.5-12.5 km depth, which covers entire Northeast China except the SLB in the center. We conjecture that the slow S-velocity belt may be associated with Cenozoic volcanism in Northeast China and is likely the result of multiple factors including a temperature anomaly, partial melts, and fluid-filled faults.
2. Our model resolves localized fast S-velocity anomalies in the crust. Particularly, the positive S-velocity anomaly below the SLB is interpreted as late-Mesozoic mafic intrusions. The high S-velocity under the CBM is attributed to middle to lower-crustal solidified magmatic intrusions.
3. Our model confirms the upper-mantle low shear velocity zones below the CBM and LXM, which support the geodynamic model of sub-lithospheric mantle melt upwellings. Additionally, our results reveal significant distinctions in lithospheric structure between the LXM and CBM, which may be associated with the differences in volcanic/magmatic activity and

basalt geochemistry in the two subregions.

4. A positive mantle S-velocity anomaly at 50-90 km depth beneath the SLB is imaged, which may reflect a depleted and more refractory lithosphere resulted from the extensive late-Mesozoic volcanism/magmatism and thus explain the absence of Cenozoic volcanism in the SLB.
5. The lithosphere-asthenosphere boundary (LAB) is evidenced by a decrease in S-wave velocity below 4.3 km/s. The LAB depth increases systematically from east to west in our study area. The LAB depth is 50-70 km beneath the CBM, 100 km beneath the SLB, and exceeds 125 km beneath the GXM.
6. In comparison with the Arabian shield and North American craton, the crust underneath Northeast China is likely rather warm (~480-970 °C between 15 and 27.5 km depth), as it is the uppermost mantle (~1200 °C), and probably associated with the active intraplate volcanism. The SLB, nonetheless, possesses a moderately warm uppermost mantle (~1080 °C).

Acknowledgements

We are grateful to the NECESSArray Project Team for sharing the waveform data of the portable seismic stations, which were downloaded from Incorporated Research Institutions for Seismology (IRIS). The teleseismic waveform data recorded by the permanent stations were provided by China Seismic Data Management Center at Institute of Geophysics, China Earthquake Administration, and can be accessed from the data center (http://www.chinarraydmc.cn). We sincerely thank Jessica Reid for her constructive comments that greatly help to improve the manuscript. The research presented in the paper is supported by the National Science Foundation of China (grant 41974011) and MOST grant (2018YFC1503606) in China. J.J. thanks the Conselho

Nacional de Desenvolvimento Científico e Tecnológico (CNPq) for his continued research fellowship (CNPq 308644/2019-0). P.M.M. is supported by funding from King Abdullah University of Science and Technology, grant number BAS/1/1339-01-01.

References

Ammon, C. J., Randall, G. E., & Zandt, G. (1990). On the nonuniqueness of receiver function inversions. *Journal of Geophysical Research: Solid Earth (1978–2012)*, *95*(B10), 15303-15318.

Berteussen, K. A. (1977). Moho depth determinations based on spectral-ratio analysis of NORSAR long-period P waves. *Physics of the Earth and Planetary Interiors*, *15*(1), 13-27.

Blackwell, D. D. (1971). The thermal structure of the continental crust, in *The Structure and Physical Properties of the Earth's Crust, Geophys. Monogr. Ser.*, vol. 14, edited by J. G. Heacock, pp. 169-184, AGU, Washington, D.C., 1971.

Chen, H., Niu, F., Obayashi, M., Grand, S. P., Kawakatsu, H., Chen, Y. J., Ning, J., & Tanaka, S. (2017). Mantle seismic anisotropy beneath NE China and implications for the lithospheric delamination hypothesis beneath the southern Great Xing'an range. *Earth and Planetary Science Letters*, *471*, 32–41.

Chen, Y., Zhang, Y., Graham, D., Su, S., & Deng, J. (2007). Geochemistry of Cenozoic basalts and mantle xenoliths in Northeast China. *Lithos*, *96*(1‐2), 108–126.

ChinaNetwork. (2006). China Seismic Network waveform data. China Earthquake Administration, doi:10.12001/ChinaNetwork.Data.

Christensen, N. I., & Mooney, W. D. (1995). Seismic velocity structure and composition of the continental crust: A global view. *Journal of Geophysical Research: Solid Earth*, *100*(B6), 9761-9788.

Deng, J., Zhao, H., Mo, X., Luo, Z., & Du, S. (1996). Continental root/plume structure in China—Key to the continental geodynamics (pp. 1–110). *Beijing: Geological*

Publishing House.

Downs, D. T., Stelten, M. E., Champion, D. E., Dietterich, H. R., Nawab, Z., Zahran, H., ... & Shawali, J. (2018). Volcanic history of the northernmost part of the Harrat Rahat volcanic field, Saudi Arabia. *Geosphere*, *14*(3), 1253-1282.

Dziewonski, A. M., & Anderson, D. L. (1981). Preliminary reference Earth model. *Physics of the earth and planetary interiors*, *25*(4), 297-356.

Ebinger, C. J., & Sleep, N. H. (1998). Cenozoic magmatism throughout east Africa resulting from impact of a single plume. *Nature*, *395*(6704), 788-791.

Fan, Q., & Hooper, P. R. (1991). The Cenozoic basaltic rocks of eastern China: Petrology and chemical composition. *Journal of Petrology*, *32*(4), 765–810.

Fan, Q., Liu, R., & Li, D. (1999). Significance of K-Ar age of bimodal volcanic rocks at Wangtian'e volcano, Changbaishan area. *Chinese Sciences Bulletin*, *44*(7): 660-663.

Fan, Q., Sui, J., Sun, Q., Li, N., & Wang, T. (2005). Preliminary research on magma mixing and explosive mechanism of the Millennium eruption of Tianchi volcano (in Chinese with English abstract). *Acta Petrologica Sinica*, *21*(6):1703-1708.

Fan, X., Chen, Q., Ai, Y., Chen, L., Jiang, M., Wu, Q., & Guo, Z. (2021). Quaternary sodic and potassic intraplate volcanism in the Northeast China controlled by the underlying heterogeneous lithospheric structures. *Geology*, *49*.

Fan, X., Chen, Q., Legendre, C. P., & Guo, Z. (2020). Intraplate volcanism and regional geodynamics in NE Asia revealed by anisotropic Rayleigh-wave tomography. *Geophysical Research Letters*, *47*.

Feng, Z., Jia, C., Xie, X., Zhang, S., Feng, Z., & Cross, T. A. (2010). Tectonostratigraphic units and stratigraphic sequences of the nonmarine Songliao basin, northeast China. *Basin Research*, *22*, 79–95.

Gosnold, W. (2011). The Global Heat Flow Database. The International Heat Flow Commission: https://ihfc-iugg.org/products/global-heat-flow-database.

Julià, J. (2007). Constraining velocity and density contrasts across the crust-mantle boundary with receiver function amplitudes. *Geophysical Journal International*, *171*(1), 286-301.

Julià, J., Ammon, C. J., & Herrmann, R. B. (2003). Lithospheric structure of the Arabian Shield from the joint inversion of receiver functions and surface-wave group velocities. *Tectonophysics*, *371*(1), 1-21.

Julià, J., Ammon, C. J., Herrmann, R. B., & Correig, A. M. (2000). Joint inversion of receiver function and surface wave dispersion observations. *Geophysical Journal International*, *143*(1), 99-112.

Julià, J., Herrmann, R. B., Ammon, C. J., & Akinci, A. (2004). Evaluation of deep sediment velocity structure in the New Madrid Seismic Zone. *Bulletin of the Seismological Society of America*, *94*, 334–340.

Julià, J., Jagadeesh, S., Rai, S. S., & Owens, T. J. (2009). Deep crustal structure of the Indian shield from joint inversion of P wave receiver functions and Rayleigh wave group velocities: Implications for Precambrian crustal evolution. *Journal of Geophysical Research: Solid Earth*, *114*, B10313.

Hammond, J., Wu, J., Ri, K., Wei, W., Yu, J., & Oppenheimer, C. (2019). Distribution of partial melt beneath Changbaishan/Paektu volcano, China/Democratic people's Republic of Korea. *Geochemistry, Geophysics, Geosystems*, *21*(1).

He, C., Dong, S., Chen, X., Santosh, M., & Niu, S. (2013). Seismic evidence for plume-induced rifting in the Songliao basin of Northeast China. *Tectonophysics*, *627*, 171–181.

Huang, J., & Zhao, D. (2006). High-resolution mantle tomography of China and surrounding regions. *Journal of Geophysical Research*, *111*, B09305.

Gao, J., Zhang, H., Zhang, S., Xin, H., Li, Z., Tian, W., Bao, F., Cheng, Z., Jia, X., & Fu, L. (2020). Magma recharging beneath the Weishan volcano of the intraplate Wudalianchi volcanic field, northeast China, implied from 3-D magnetotelluric imaging. *Geology*, *48*.

Ge, X. H., & Ma, W. P. (2007). Mesozoic-Cenozoic tectonic framework of southern Northeast Asia. *Geology in China*, *34*, 212–228.

Guo, Z., Chen, Y. J., Ning, J., Feng, Y., Grand, S. P., Niu, F., Kawakatsu, H., Tanaka, S., Obayashi, M., & Ni, J. F. (2015). High resolution 3-D crustal structure beneath NE China from joint inversion of ambient noise and receiver functions using NECESSArray data. *Earth and Planetary Science Letters*, *416*, 1–11.

Guo, Z., Chen, Y. J., Ning, J., Yang, Y., Afonso, J. C., & Tang, Y. (2016). Seismic evidence of on-going sublithosphere upper mantle convection for intra-plate volcanism in Northeast China. *Earth and Planetary Science Letters*, *433*, 31–43.

Guo, Z., Wang, K., Yang, Y., Tang, Y., Chen, Y. J., & Hung, S.-H. (2018). The origin and mantle dynamics of quaternary intraplate volcanism in Northeast China from joint inversion of surface wave and body wave. *Journal of Geophysical Research: Solid Earth*, *123*.

Kern, H., & Richter, A. (1981). Temperature derivatives of compressional and shear-wave velocities in crustal and mantle rocks at 6 kbar confining pressure. *Journal of Geophysics-Zeitschrift fur Geophysik*, *49*(1), 47–56.

Kyong-Song, R., Hammond, J. O. S., Chol-Nam, K., Hyok, K., Yong-Gun, Y., Gil-Jong, P., Chong-Song, R.,Oppenheimer, C., Liu, K. W., Iacovino, K., & Kum-Ran, R. (2016). Evidence for partial melt in the crust beneath Mt. Paektu (Changbaishan), Democratic People’s Republic of Korea and China. *Science Advances*, *2*(4), e1501513.

Langston, C. A. (1979). Structure under Mount Rainier, Washington, inferred from teleseismic body waves. *Journal of Geophysical Research: Solid Earth (1978–2012)*, *84*(B9), 4749-4762.

Laske, G., Masters, G., Ma, Z., & Pasyanos, M. (2013). Update on CRUST1.0 – A 1-degree Global Model of Earth’s Crust. *EGU General Assembly Conference Abstract*, *15*, 2658.

Lei, J., & Zhao, D. (2005). P-wave tomography and origin of the Changbai intraplate volcano in Northeast Asia. *Tectonophysics*, *397*(3-4), 281–295.

Li, C., & Van der Hilst, R. D. (2010). Structure of the upper mantle and transition zone beneath Southeast Asia from traveltime tomography. *Journal of Geophysical Research*, *115*, B07308.

Li, J., & Niu, F. (2010). Seismic anisotropy and mantle flow beneath northeast China inferred from regional seismic networks. *Journal of Geophysical Research*, *115*, B12327.

Li, S., Guo, Z., & Chen, Y. (2017). Complicated 3D mantle flow beneath Northeast China from shear wave splitting and its implication for the Cenozoic intraplate volcanism. *Tectonophysics*, *709*, 1–8.

Li, Y., Wu, Q., Pan, J., & Sun, L. (2012). S-wave velocity structure of northeastern china from joint inversion of Rayleigh wave phase and group velocities. *Geophysical Journal International*, *190*, 105-115.

Li, Y., Wu, Q., Pan, J., Zhang, F., & Yu, D. (2013). An upper-mantle S-wave velocity model for East Asia from Rayleigh wave tomography. *Earth and Planetary Science Letters*, *377-378*, 367-377.

Li, Z., Ni, S., Zhang, B., Bao, F., Zhang, S., Deng, Y., & Yuen, D. A. (2016). Shallow magma chamber under the Wudalianchi Volcanic Field unveiled by seismic imaging with dense array. *Geophysical Research Letters*, *43*, 4954–4961.

Ligorría, J. P., & Ammon, C. J. (1999). Iterative deconvolution and receiver-function estimation. *Bulletin of the seismological Society of America*, *89*(5), 1395-1400.

Liu, H., & Niu, F. (2011). Receiver function study of the crustal structure of Northeast China: Seismic evidence for a mantle upwelling beneath the eastern flank of the Songliao Basin and the Changbaishan region. *Earthquake Science*, *24*: 27-33.

Liu, J. (1987). Study on geochronology of the Cenozoic volcanic rocks in Northeast China (in Chinese with English abstract). *Acta Petrologica Sinica*, (4): 21-31.

Liu, J., Han, J., & Fyfe, W. S. (2001). Cenozoic episodic volcanism and continental rifting in northeast China and possible link to Japan Sea development as revealed from K-Ar geochronology. *Tectonophysics*, *339*(3-4), 385–401.

Liu, Z., Huang, J., & Yao, H. (2016). Anisotropic Rayleigh wave tomography of Northeast China using ambient seismic noise. *Physics of the Earth and*

Planetary Interiors, *256*, 37-48.

Ma, J., Tian, Y., Liu, C., Zhao, D., Feng, X., & Zhu, H. (2018). P-wave tomography of Northeast Asia: Constraints on the western Pacific plate subduction and mantle dynamics. *Physics of the Earth and Planetary Interiors*, *274*, 105–126.

Meng, Q. (2003). What drove late Mesozoic extension of the northern China-Mongolia tract? *Tectonophysics*, *369*(3-4), 155–174.

Oh, C. W. (2006). A new concept on tectonic correlation between Korea, China and Japan: histories from the late Proterozoic to Cretaceous. *Gondwana Research*, *9*, 47–61.

Ohtani, E., Litasov, K., Hosoya, T., Kubo, T., & Kondo, T. (2004). Water transport into the deep mantle and formation of a hydrous transition zone. *Physics of the Earth and Planetary Interiors*, *143*, 255–269.

Owens, T. J., Zandt, G., & Taylor, S. R. (1984). Seismic evidence for an ancient rift beneath the Cumberland Plateau, Tennessee: A detailed analysis of broadband teleseismic P waveforms. *Journal of Geophysical Research: Solid Earth (1978–2012)*, *89*(B9), 7783-7795.

Pan, J., Wu, Q., Li, Y., & Yu, D. (2014). Ambient noise tomography in northeast China (in Chinese with English abstract). *Chinese Journal of Geophysics*, *57*: 812-821.

Pan, J., Li, Y., Wu, Q., & Yu, D. (2015). 3-D S-wave velocity structure of crust and upper-mantle beneath the northeast China (in Chinese with English abstract). *Chinese Journal of Geophysics*, *57*(7): 2077-2087.

Plank, T., & Forsyth, D. W. (2016). Thermal structure and melting conditions in the mantle beneath the Basin and Range province from seismology and petrology. *Geochemistry, Geophysics, Geosystems*, *17*, 1312–1338.

Qiang, Z., & Wu, Q. (2015). Upper mantle anisotropy beneath the north of northeast China and its dynamic significance (in Chinese with English abstract). *Chinese Journal of Geophysics*, *58*, 3540–3552.

Ren, J., Tamaki, K., Li, S., & Junxia, Z. (2002). Late Mesozoic and Cenozoic rifting and its dynamic setting in Eastern China and adjacent areas. *Tectonophysics*, *344*, 175–205.

Savage, M. K. (1998). Lower crustal anisotropy or dipping boundaries? Effects on receiver functions and a case study in New Zealand. *Journal of Geophysical Research: Solid Earth*, *103*(B7), 15069-15087.

Şengör, A. M. C., NatalIn, B. A., & Burtman, V. S. (1993). Evolution of the Altaid tectonic collage and Palaeozoic crustal growth in Eurasia. *Nature*, *364*(6435): 299-307.

Shen, W., & Ritzwoller, M. H. (2016). Crustal and uppermost mantle structure beneath the United States. *Journal of Geophysical Research: Solid Earth*, *121*.

Sumino, Y., & Anderson, O.L. (1982). Elastic constants in minerals. In: Carmichel, R.S. (Ed.), CRC Handbook of Physical Properties of Rocks. *CRC Press*, *Boca Raton*, *FL*, pp. 39–138.

Tang, J., Deng, Q., Zhao, G., Bai, D., Jin, G., Li, W., Xuan, F., Zhan, Y., Li, G., Hong, F., & Ma, M. (2001). Electric conductivity and magma chamber at the Tianchi volcano area in Changbaishan Mountain, *Seismology and Geology*, *23*, 191–200.

Tang, Y., Obayashi, M., Niu, F., Grand, S. P., Chen, Y. J., Kawakatsu, H., Tanaka, S., Ning, J., & Ni, J. F. (2014). Changbaishan volcanism in northeast China linked to subduction-induced mantle upwelling. *Nature Geoscience*, *7*(6), 470–475.

Tang, Z., Julià, J., Zahran, H., & Mai, P. M. (2016). The lithospheric shear-wave velocity structure of Saudi Arabia: Young volcanism in an old shield. *Tectonophysics*, *680*, 8-27.

Tang, Z., Mai, P. M., Julià, J., & Zahran, H. (2019). Shear velocity structure beneath Saudi Arabia from the joint inversion of P and S wave receiver functions, and Rayleigh wave group-velocity dispersion data. *Journal of Geophysical Research: Solid Earth*, *124*.

Tao, K., Niu, F., Ning, J., Chen, Y. J., Grand, S., Kawakatsu, H., Tanaka, S., Obayashi, M., & Ni, J. (2014). Crustal structure beneath NE China imaged by NECESSArray receiver function data. *Earth and Planetary Science Letters*, *398*, 48–57.

Tao, K., Grand, S. P., & Niu, F. (2018). Seismic structure of the upper mantle beneath eastern Asia from full waveform seismic tomography. *Geochemistry, Geophysics, Geosystems*, *19*, 2732–2763.

Tian, Y., Zhu, H., Zhao, D., Liu, C., Feng, X., Liu, T., & Ma, J. (2016). Mantle transition zone structure beneath the Changbai volcano: Insight into deep slab dehydration and hot upwelling near the 410 - km discontinuity. *Journal of Geophysical Research: Solid Earth*, *121*, 5794–5808.

Wang, F., Zhou, X., Zhang, L., Ying, J., Zhang, Y., Wu, F., & Zhu, R. (2006). Late Mesozoic volcanism in the Great Xing'an Range (NE China): Timing and implications for the dynamic setting of NE Asia. *Earth and Planetary Science Letters*, *251*(1-2), 179–198.

Wang, T., Feng, J., Liu, K. H., & Gao, S. S. (2019). Crustal structure beneath the Malawi and Luangwa Rift Zones and adjacent areas from ambient noise tomography. *Gondwana Research*, *67*, 187-198.

Wei, H., Liu, J., & Meng, Q. (2010). Structural and sedimentary evolution of the southern Songliao Basin, northeast China, and implications for hydrocarbon prospectivity. *American Association of Petroleum Geologists Bulletin*, *94*(4), 533–566.

Wei, W., Hammond, J. O. S., Zhao, D., Xu, J., Liu, Q., & Gu, Y. (2019). Seismic evidence for a mantle transition zone origin of the Wudalianchi and Halaha volcanoes in northeast China. *Geochemistry, Geophysics, Geosystems*, *20*, 398–416.

Wei, W., Xu, J., Zhao, D., & Shi, Y. (2012). East Asia mantle tomography: New insight into plate subduction and intraplate volcanism. *Journal of Asian Earth Sciences*, *60*, 88–103.

Wei, W., Zhao, D., Xu, J., Wei, F., & Liu, G. (2015). P and S wave tomography and anisotropy in Northwest Pacific and East Asia: Constraints on stagnant slab and intraplate volcanism. *Journal of Geophysical Research: Solid Earth*, *120*, 1642–

1666.

Wu, F., Jahn, B. M., Wilde, S. A., Lo, C., Yui, T., Lin, Q., Ge, W., & Sun, D. (2003). Highly fractionated I-type granites in NE China (I): geochronology and petrogenesis. *Lithos*, *66*: 241–273.

Wu, F., Lin, J., Wilde, S. A., Zhang, X., & Yang, J. (2005). Nature and significance of the Early Cretaceous giant igneous event in eastern China. *Earth and Planetary Science Letters*, *233*(1-2), 103–119.

Wu, F., Sun, D., Ge, W., Zhang, Y., Grant, M. L., Wilde, S. A., & Jahn, B. M. (2011). Geochronology of the Phanerozoic granitoids in northeastern China. *Journal of Asian Earth Sciences*, *41*, 1–30.

Wu, Q., Zheng, X., Pan, J., Zhang, F., & Zhang, G. (2009). Measurement of interstation phase velocity by wavelet transformation, *Earthquake Science*, *22*, 425–429.

Yu, Y., Song, J., Liu, K. H., & Gao, S. S. (2015). Determining crustal structure beneath seismic stations overlying a low-velocity sedimentary layer using receiver functions. *Journal of Geophysical Research: Solid Earth*, *120.*

Zelt, B. C., & Ellis, R. M. (1999). Receiver-function studies in the Trans Hudson Orogen, Saskatchewan. *Canadian Journal of Earth Sciences, 36,* 585–603.

Zhan, Y., Zhao, G., Wang, J., Xiao, Q., Tang, J. & Rokityansky, II. (2006). Crustal electric conductivity structure for Wudalianchi volcanic cluster in the Heilongjiang Province. China. *Acta Petrologica Sinica*, *22*, 1494–1502.

Zhang, C., Zhang, X., Zhao, J., Liu, B., Zhang, J., Yang, Z., Hai, Y. & Sun, G. (2002). Crust–mantle structure of the Changbaishan Tianchi volcanic region and its vicinity: an exploratory study and inferences. *Chinese Journal of Geophysics*, *45*, 862– 871.

Zhang, F., Wu, Q., & Li, Y. (2013). The traveltime tomography study by teleseismic P wave data in the Northeast China area (in Chinese with English abstract). *Chinese Journal of Geophysics*, *56*, 2690–2700.

Zhang, G., Wu, Q., Pan, J., Zhang, F., & Yu, D. (2013). Study of crustal structure and

Possion ration of NE China by H-K stack and CCP stack methods (in Chinese with English abstract). *Chinese Journal of Geophysics*, *56*, 4084–4094.

Zhang, J., Gao, S., Ge, W., Wu, F., Yang, J., Wilde, S. A., & Li, M. (2010). Geochronology of the Mesozoic volcanic rocks in the Great Xing'an Range, northeastern China: Implications for subduction - induced delamination. *Chemical Geology*, *276*(3-4), 144–165.

Zhang, R., Wu, Q., Sun, L., He, J., & Gao, Z. (2014). Crustal and lithospheric structure of Northeast China from S-wave receiver functions. *Earth and Planetary Science Letters*, *401*, 196–205.

Zhao, D., Lei, J., & Tang, R. (2004). Origin of the Changbai intraplate volcanism in Northeast China: evidence from seismic tomography, *China Science Bulletin*, *49*, 1401–1408.

Zhao, D., & Ohtani, E. (2009). Deep slab subduction and dehydration and their geodynamic consequences: evidence from seismology and mineral physics. *Gondwana Research*, *16*, 401–413.

Zhao, D., & Tian, Y. (2013). Changbai intraplate volcanism and deep earthquakes in East Asia: A possible link? *Geophysical Journal International*, *195*(2), 706–724.

Zhao, D., Tian, Y., Lei, J., Liu, L., & Zheng, S. (2009). Seismic image and origin of the Changbai intraplate volcano in East Asia: Role of big mantle wedge above the stagnant Pacific slab. *Physics of the Earth and Planetary Interiors*, *173*(3-4), 197–206.

Zhao, D., Yanada, T., Hasegawa, A., Umino, N., & Wei, W. (2012). Imaging the subducting slabs and mantle upwelling under the Japan Island. *Geophysical Journal International*, *190*(2), 816–828.

Zhou, J., & Wilde, S.A. (2013). The crustal accretion history and tectonic evolution of the NE China segment of the Central Asian Orogenic Belt. *Gondwana Research*, *23*, 1365–1377.

Figures & Captions

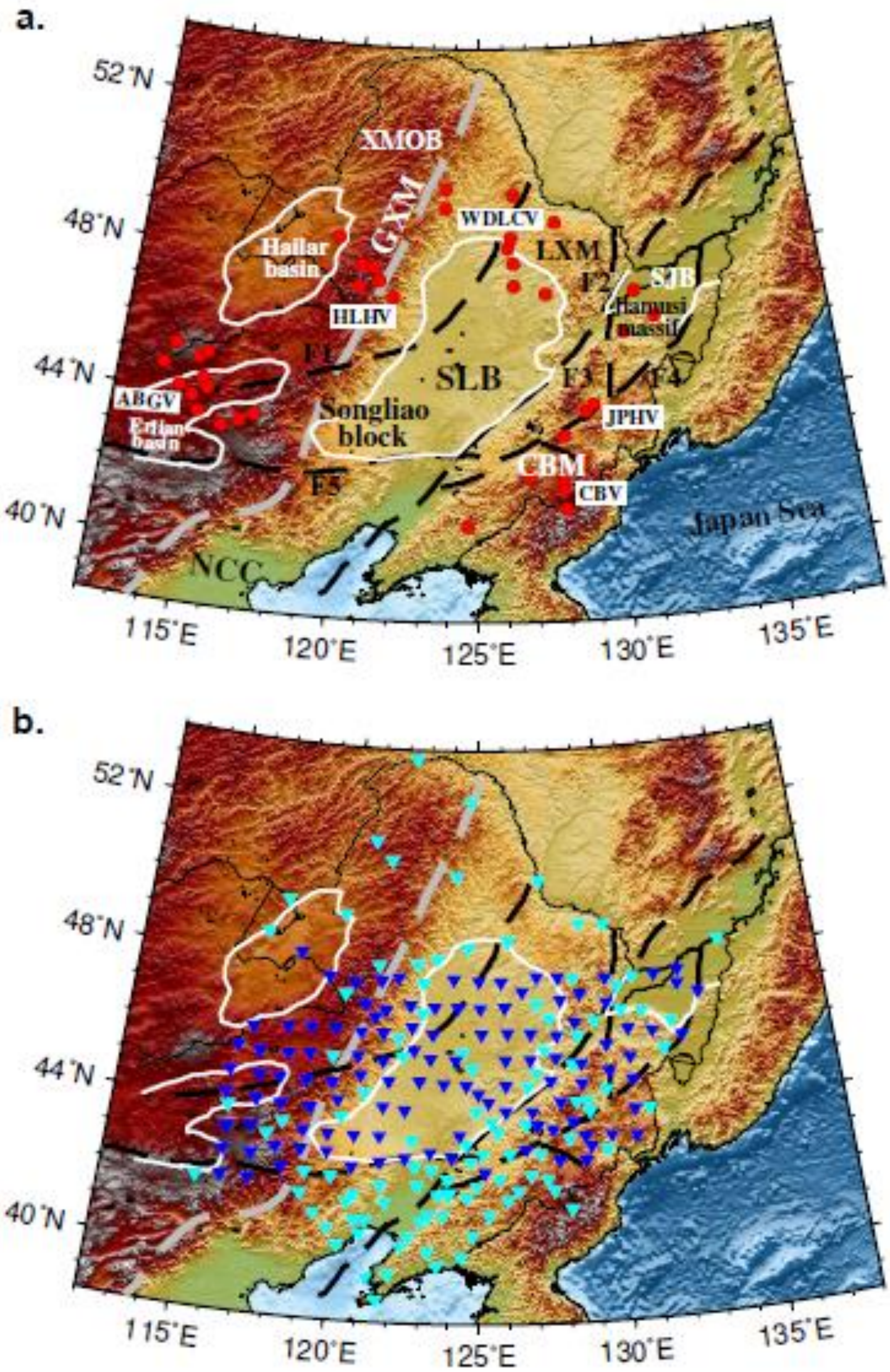

Figure 1. (a) Topographic map of Northeast China and its adjacent areas, showing major geological features and Quaternary volcanoes (red points). Dashed black lines F1-F5 represent the Nenjiang (NJF), Mudanjiang (MDJF), Yilan-Yitong (YYF), Dunhua-Mishan (DMF), and Chifeng-Kaiyuan faults (CKF), respectively. The North South

Gravity Lineament (NSGL) is depicted by a dash gray line. White lines outline the main sedimentary basins in the region. CBM = Changbai mountains; GXM = Greater Xing'an mountain range; LXM = Lesser Xing'an mountain range; SJB = Sanjiang basin; SLB = Songliao basin; NCC = North China craton; XMOB = Xingmeng Orogenic Belt; CBV = Changbaishan volcano; JPHV = Jingpohu volcano; WDLCV = Wudalianchi volcano; HLHV = Halaha volcano; ABGV = Abaga volcano. (b) Distribution of 225 seismic stations comprising 107 CEA permanent stations (cyan inverted triangles) and 118 NECESSArray temporary sites (blue inverted triangles) used in our study.

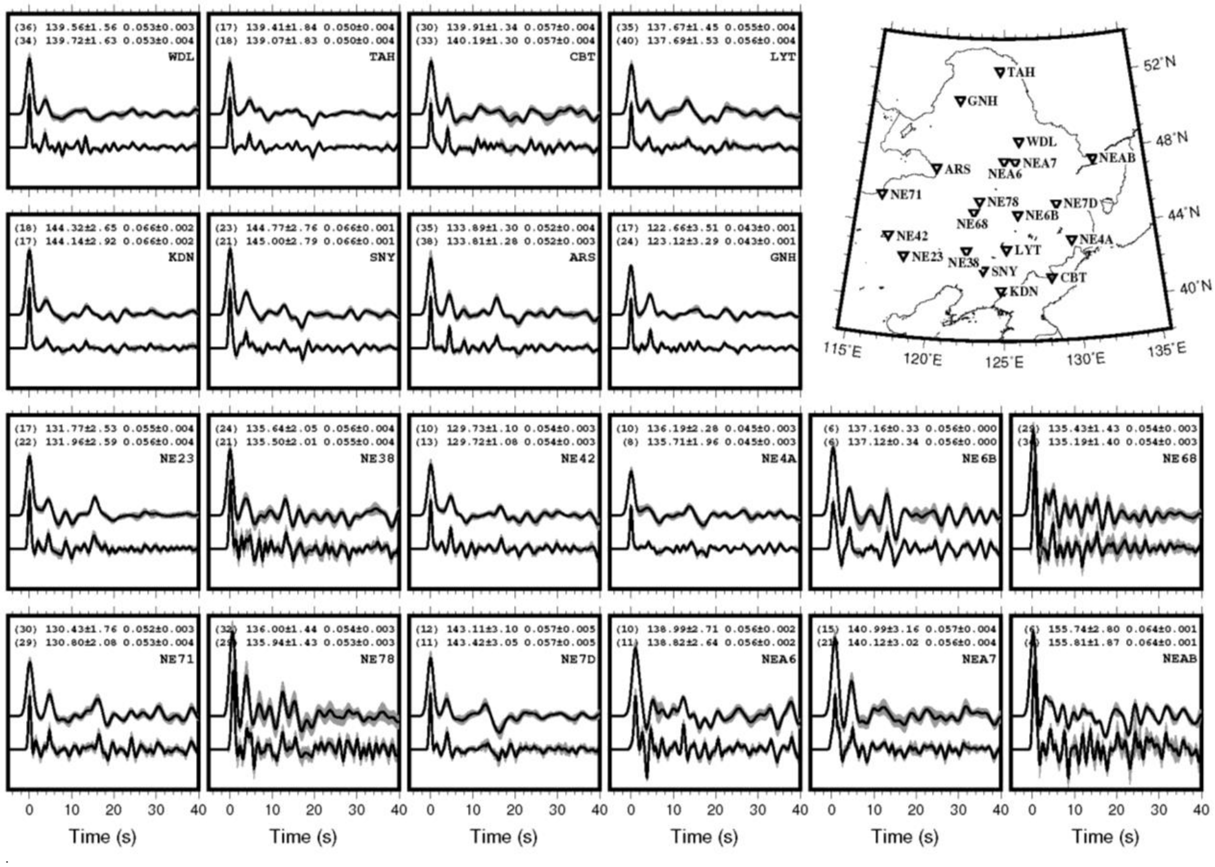

Figure 2. Radial receiver function averages at two Gaussian widths of α = 1.0 and 2.5 for a small selection of stations (marked by inverted triangles in the right map). Black time series manifest the average receiver functions, while gray-shaded swaths indicate the confidence bounds. The number of receiver functions in each stack, the average event back-azimuth (with variation, in degree), the average ray-parameter (with

variation, in second per kilometer), and the station name are shown in each panel.

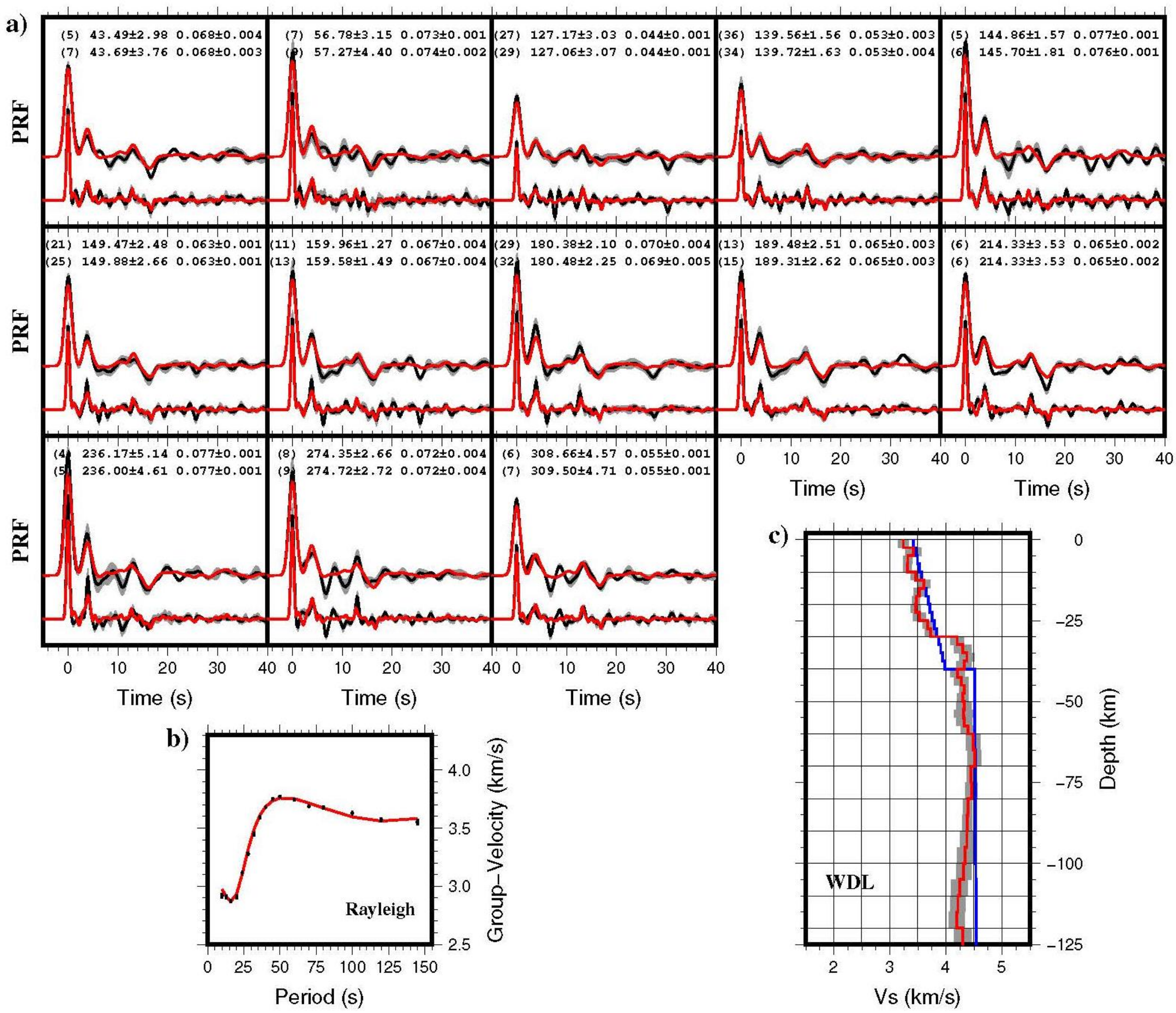

Figure 3. Joint inversion of receiver function averages and Rayleigh wave group velocities at station WDL. In panels (a), black and red lines represent the observed (with gray-shaded confidence bounds) and predicted receiver functions, respectively. The number of receiver functions for each cluster, the average back-azimuth (with variation, in degree), and the average ray-parameter (with variation, in second per kilometer) are exhibited. The observed and predicted Rayleigh wave group velocities (period range 10 to 145 s) are represented by black points and red curve in panel (b). The 1-D inverted shear-wave velocity model (red, with gray-shaded confidence bounds) and the initial model (blue) are visualized in panel (c).

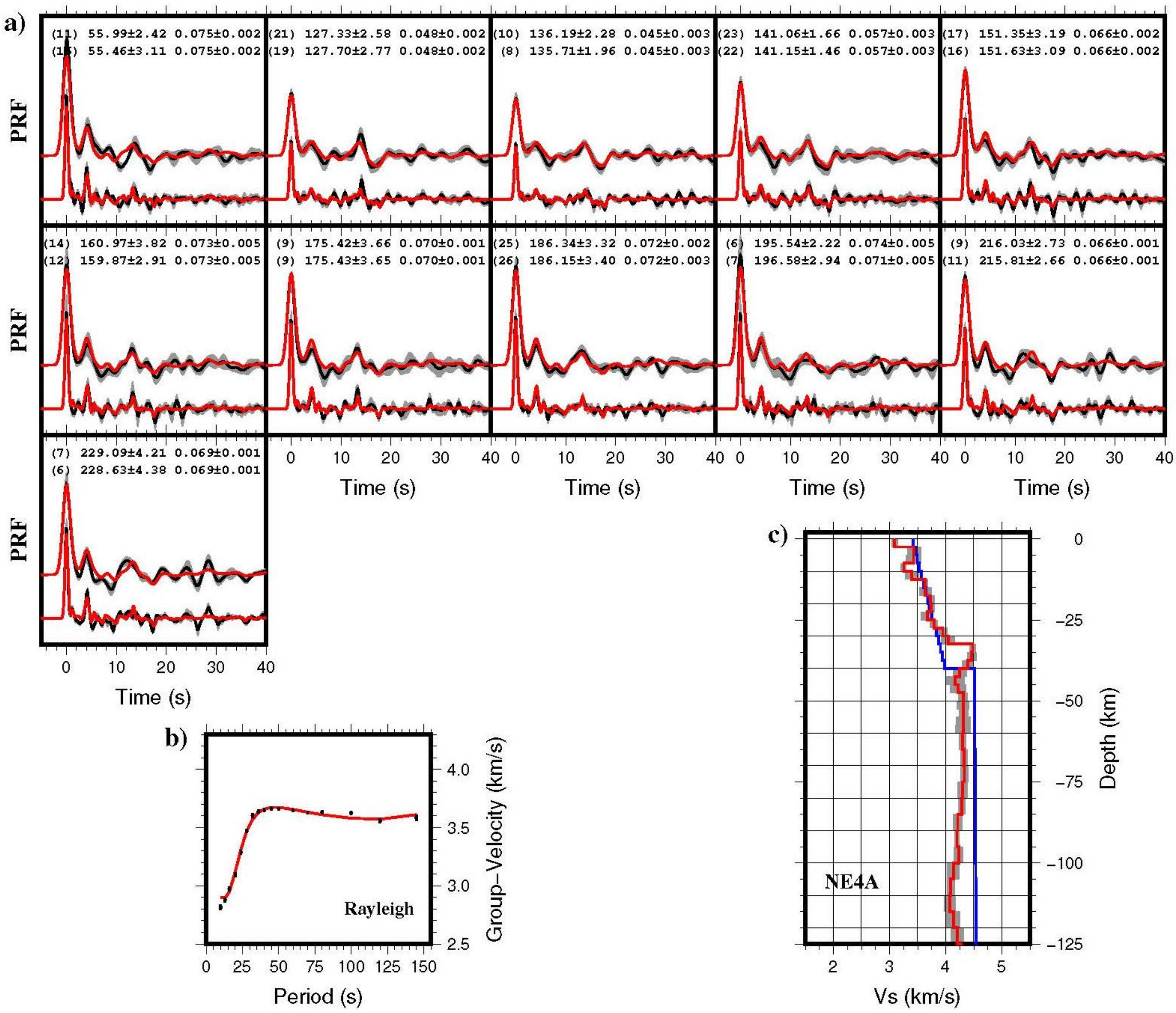

Figure 4. Same as Figure 3 but for station NE4A.

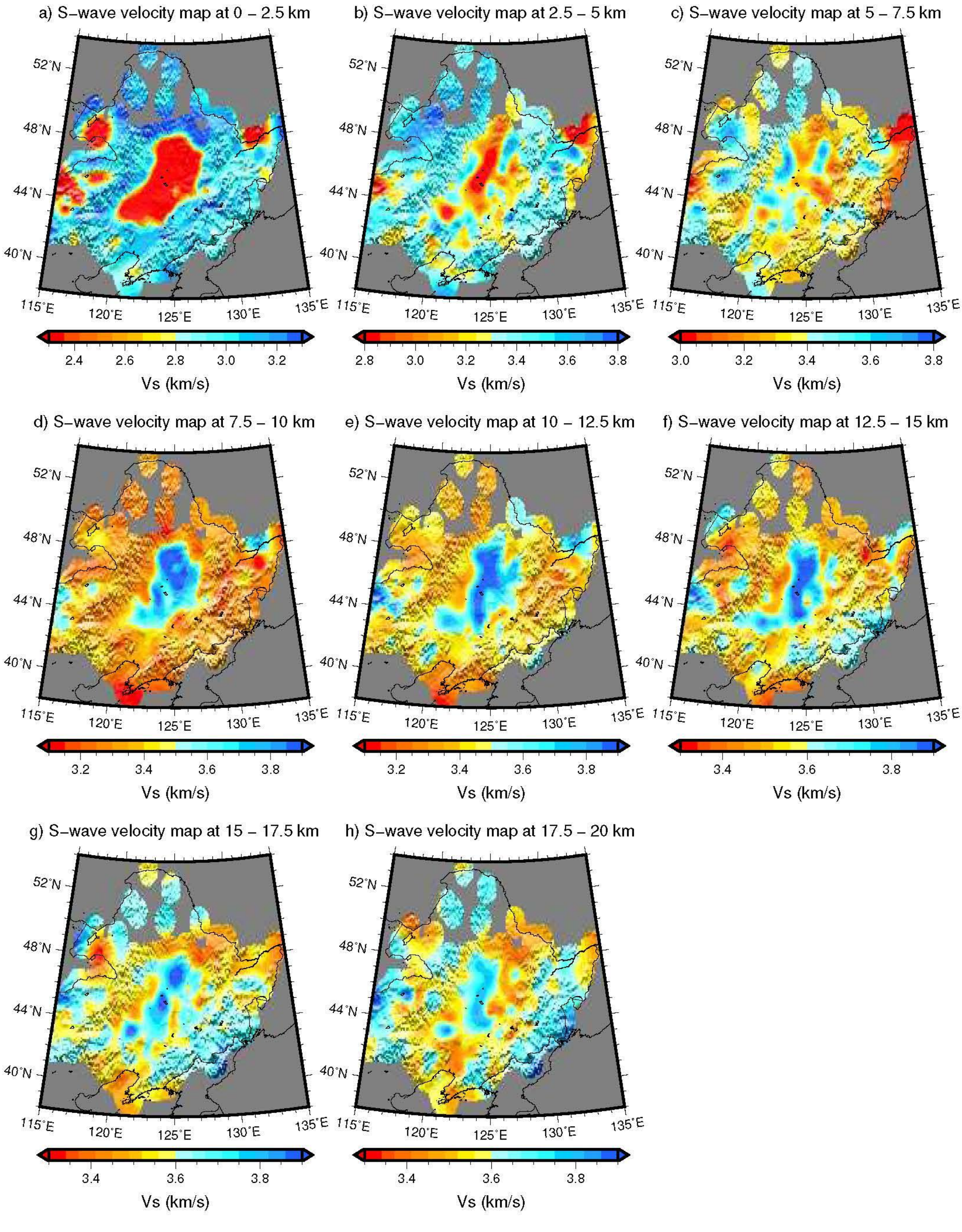

Figure 5. Horizontal slices of shear-wave velocities at upper-crustal depths (0-20 km)

beneath Northeast China. Note that color scale changes for each map to enhance lateral velocity contrasts.

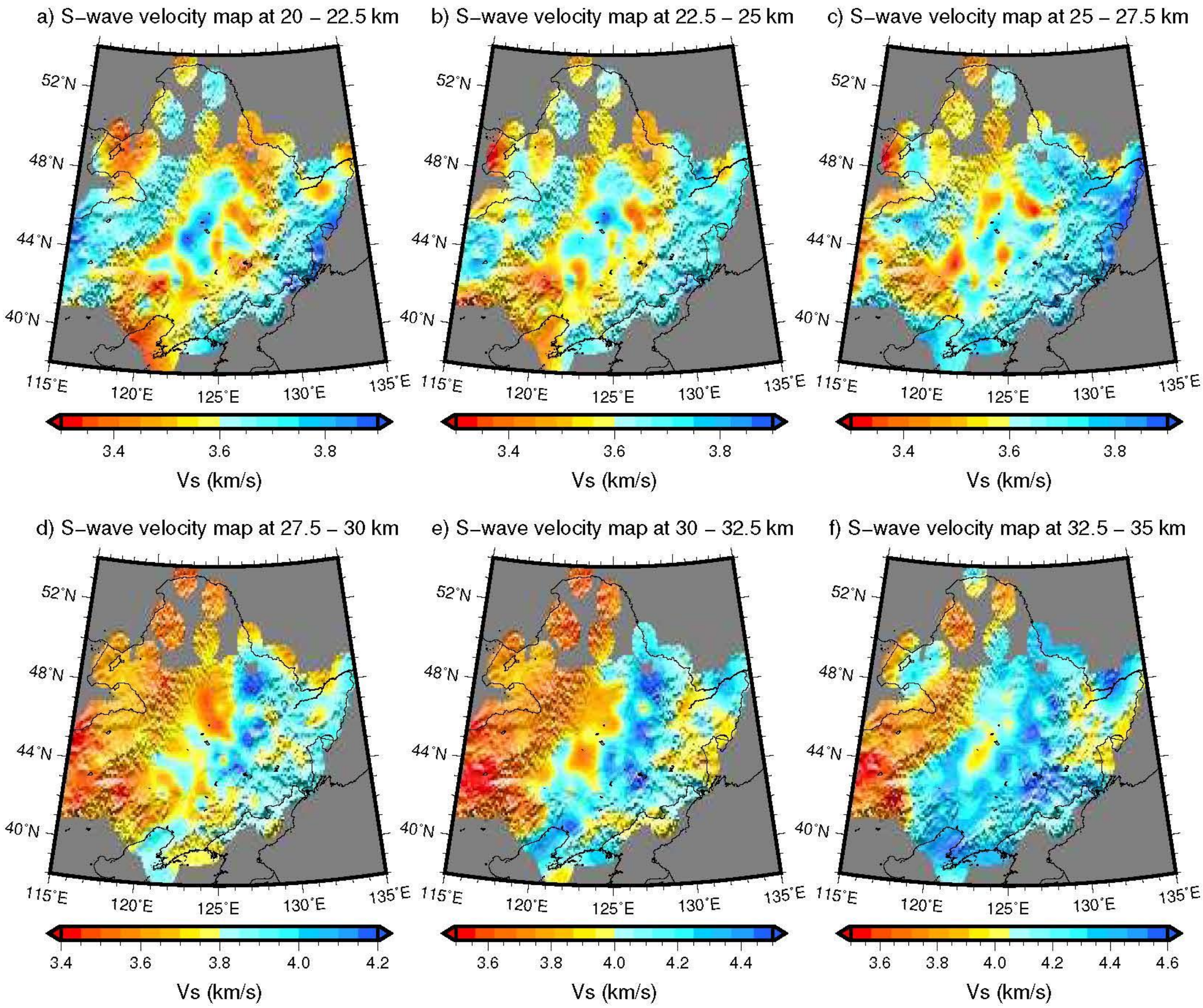

Figure 6. Horizontal slices of S-wave velocities at lower-crustal and Moho depths (20-50 km) below Northeast China.

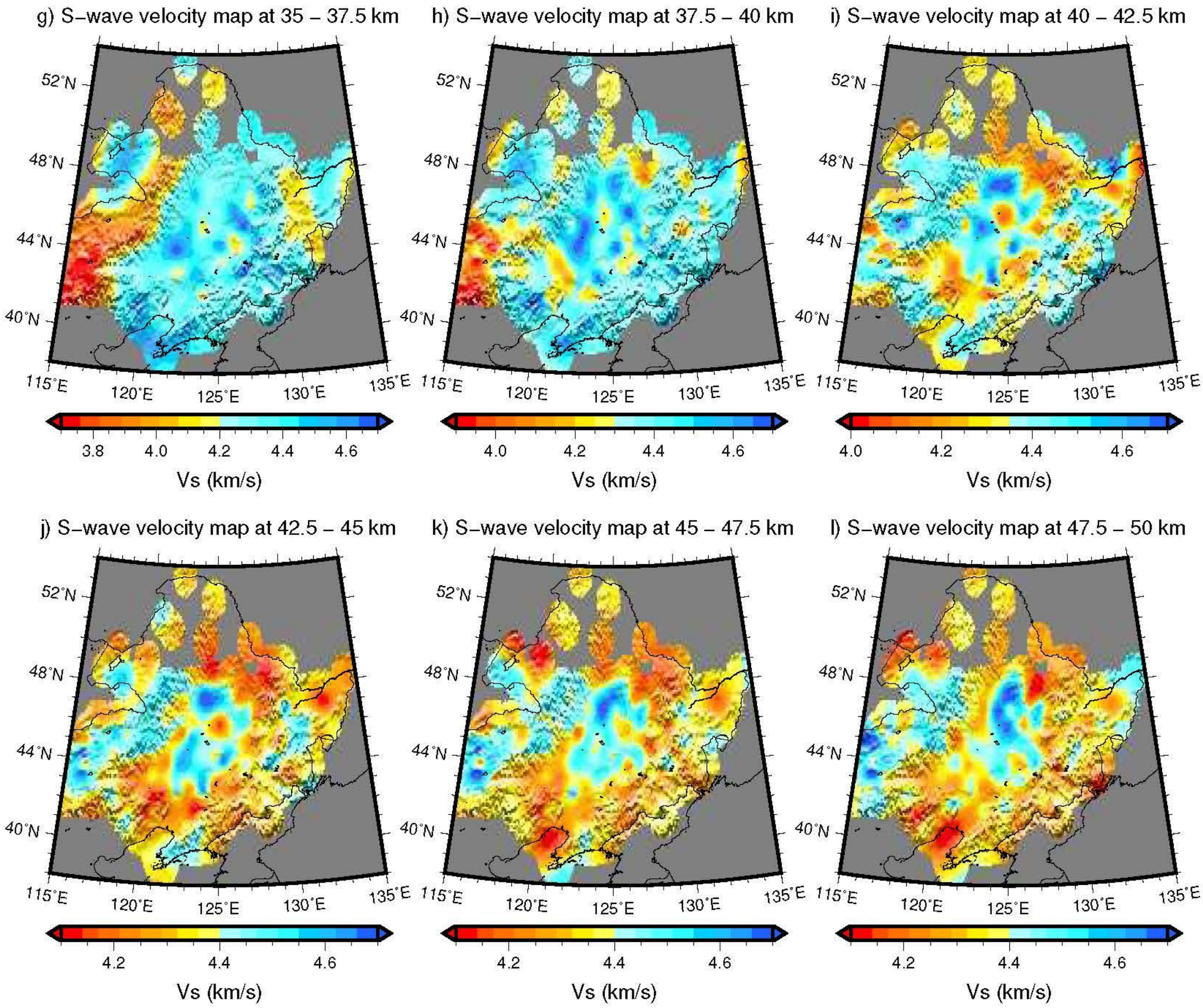

Figure 6 (continued).

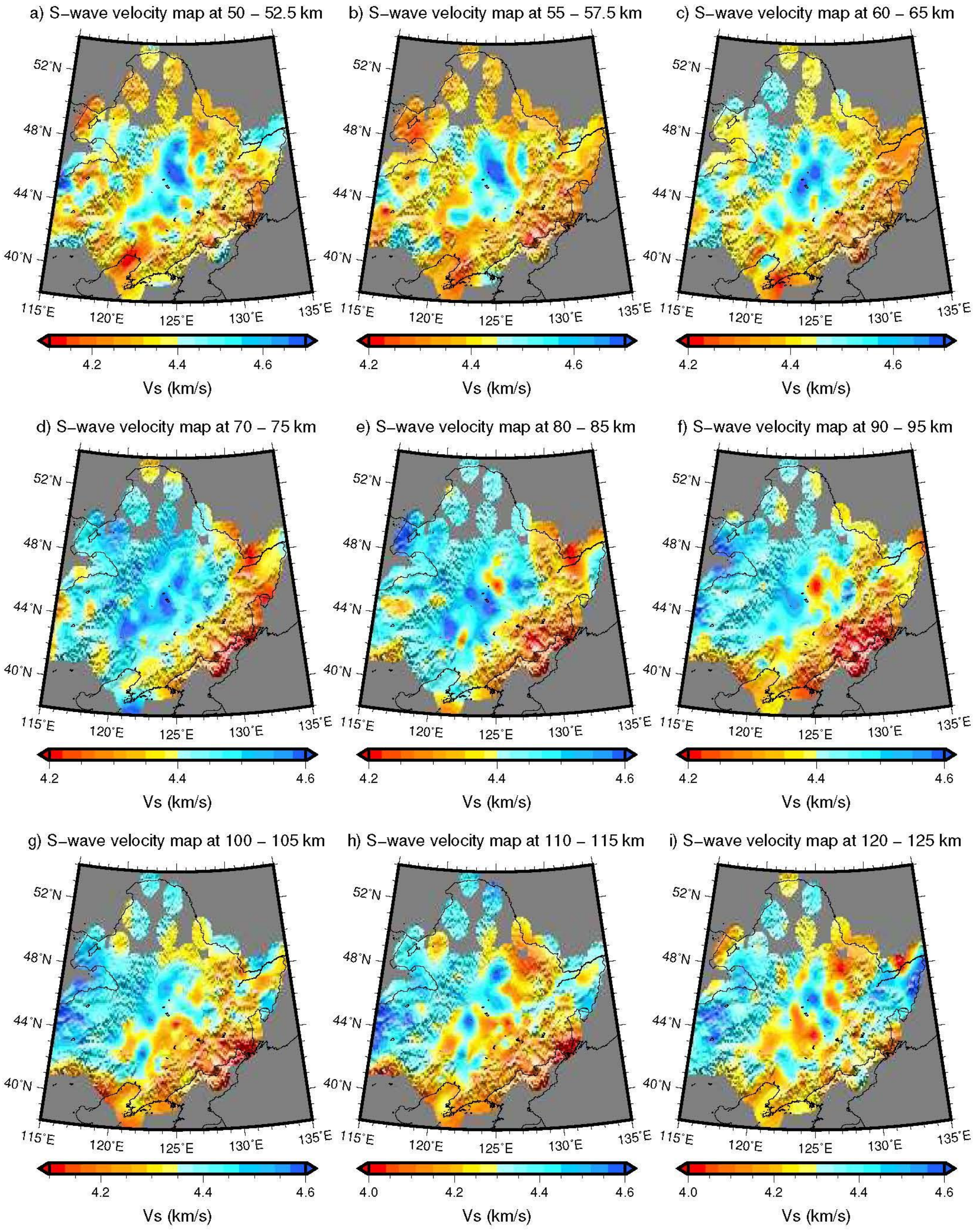

Figure 7. Horizontal slices of S-wave velocities at upper-mantle depths (50-125 km).

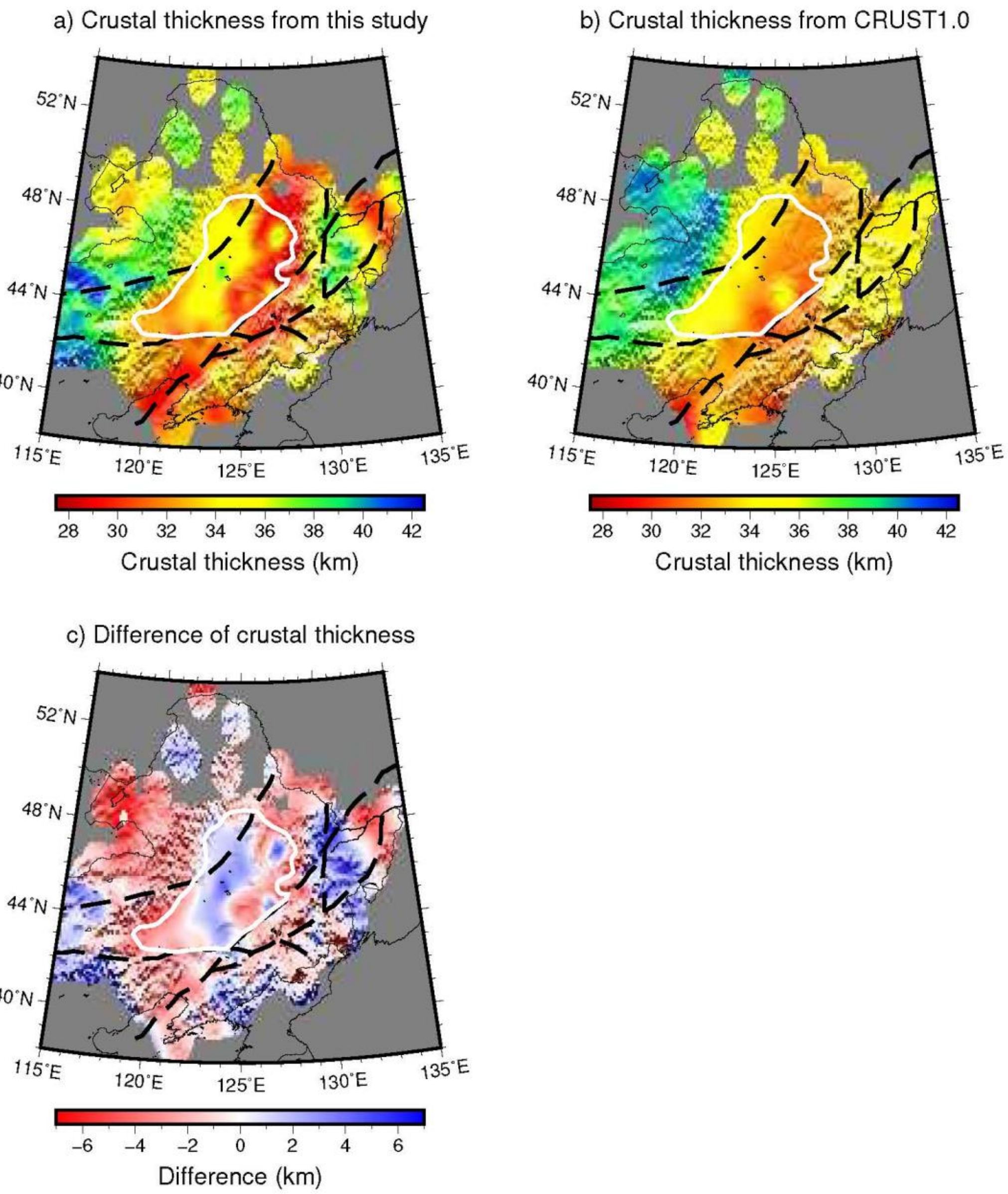

Figure 8. Comparison of the crustal thickness map obtained in this study with the crustal thickness from CRUST1.0. Panel c shows the differences between our results and CRUST1.0.

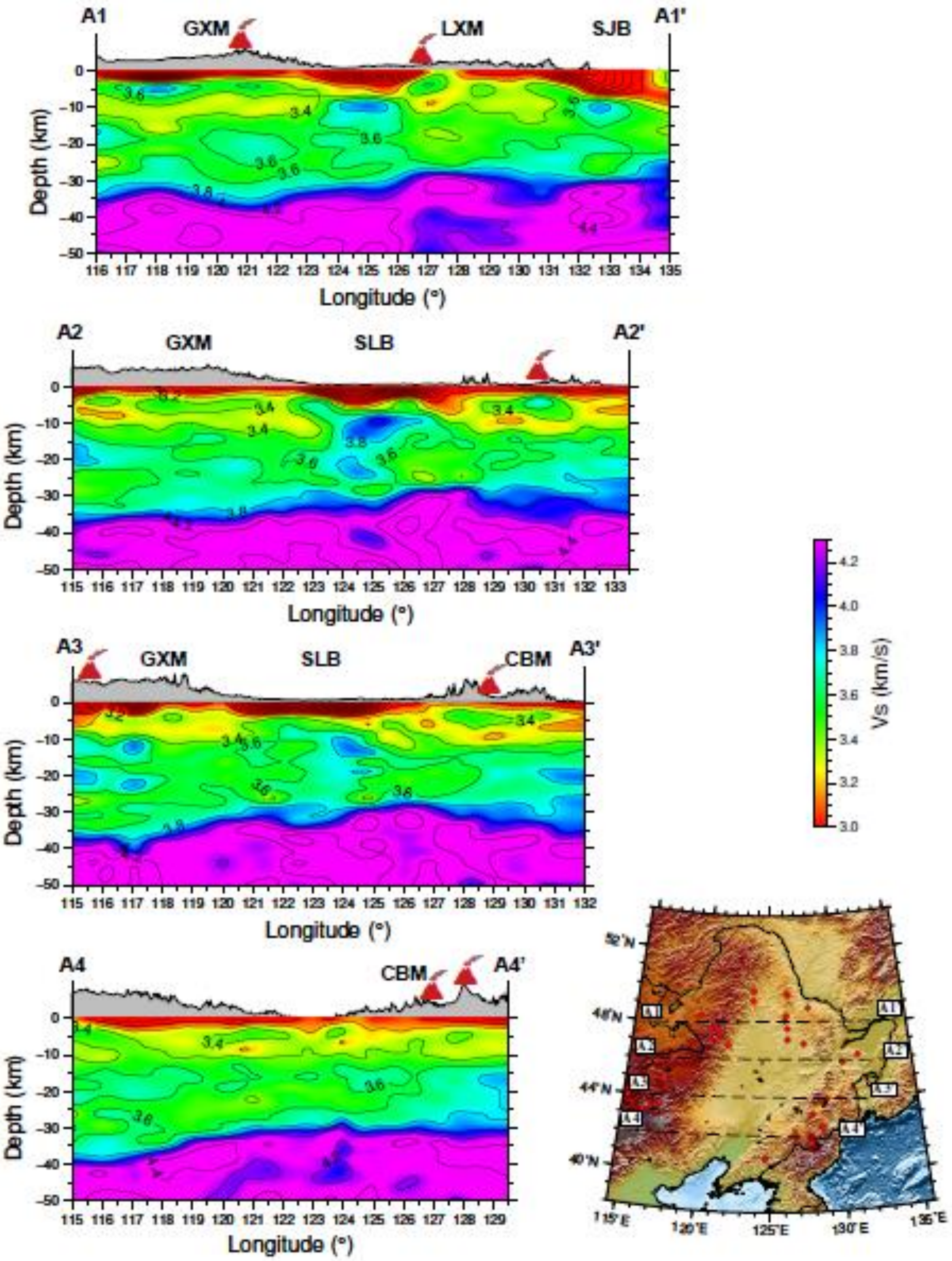

Figure 9. Vertical slices of shear-wave velocity along profiles A1–A4 across Northeast China over the crustal depths (0–50 km). Red points in the map indicate Quaternary volcanoes. CBM = Changbai mountains; GXM = Greater Xing'an mountain range; LXM = Lesser Xing'an mountain range; SJB = Sanjiang basin; SLB = Songliao basin.

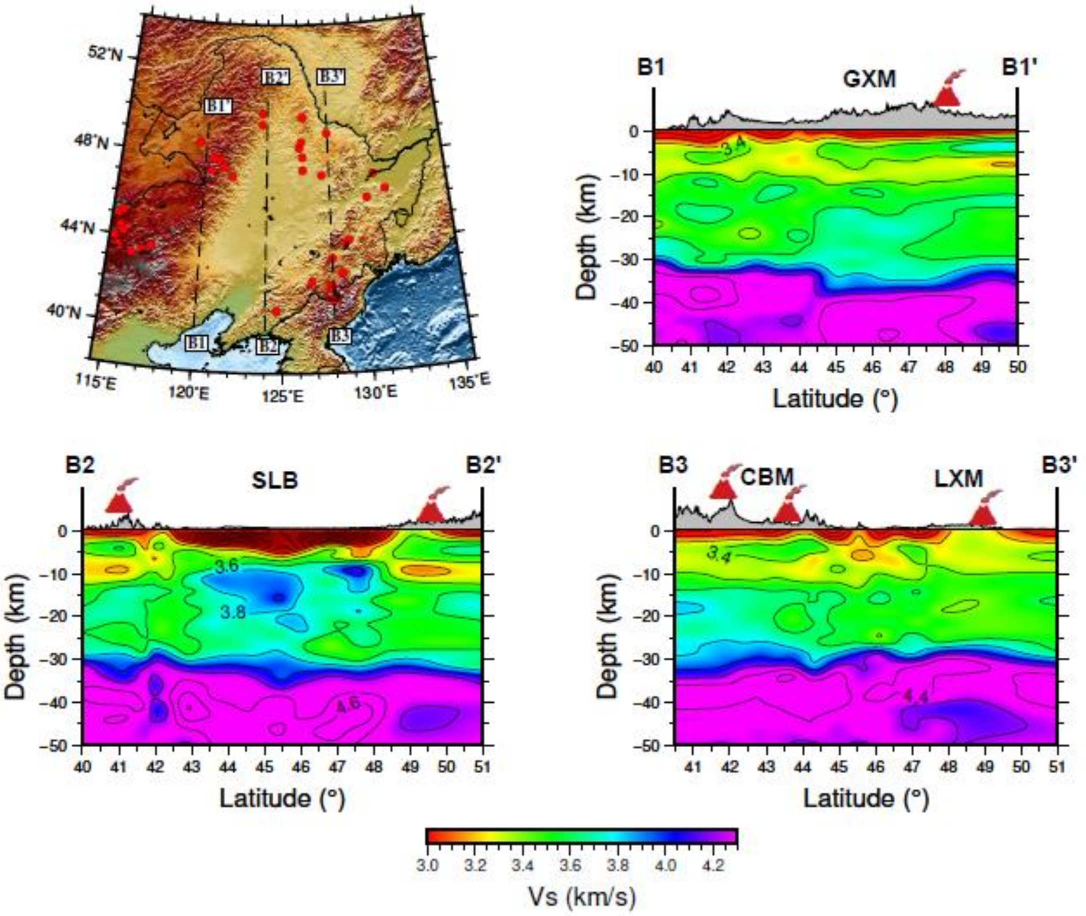

Figure 10. Vertical transects through the shear-wave velocity model along profiles B1–B3 across Northeast China for the crustal levels (0–50 km). Red points in the map represent Quaternary volcanoes. CBM = Changbai mountains; GXM = Greater Xing'an mountain range; LXM = Lesser Xing'an mountain range; SLB = Songliao basin.

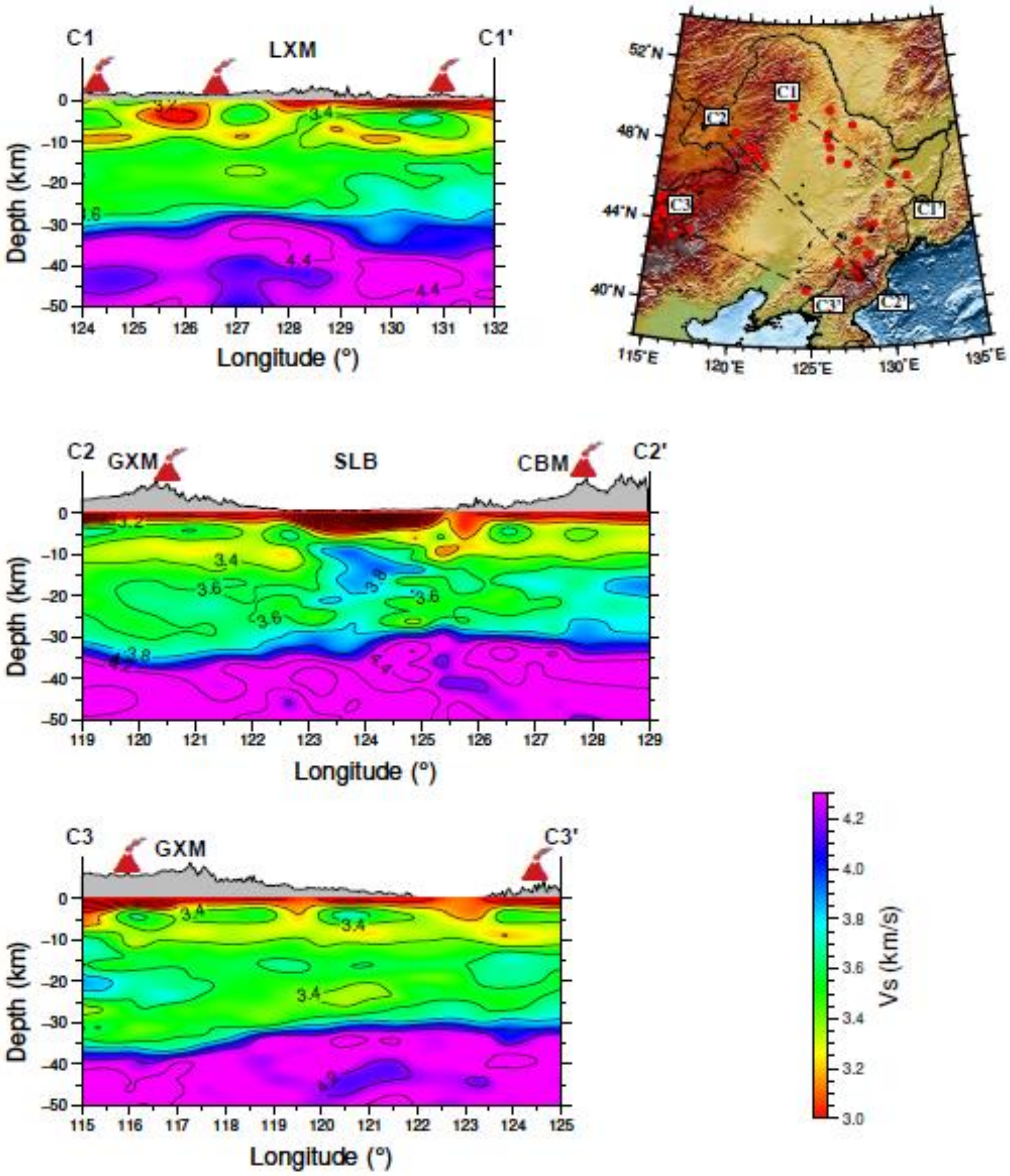

Figure 11. Vertical shear-wave velocity transects along profiles C1–C3 over the depth range of 0–50 km. Quaternary volcanoes are marked as red points in the map. CBM = Changbai mountains; GXM = Greater Xing'an mountain range; LXM = Lesser Xing'an mountain range; SLB = Songliao basin.

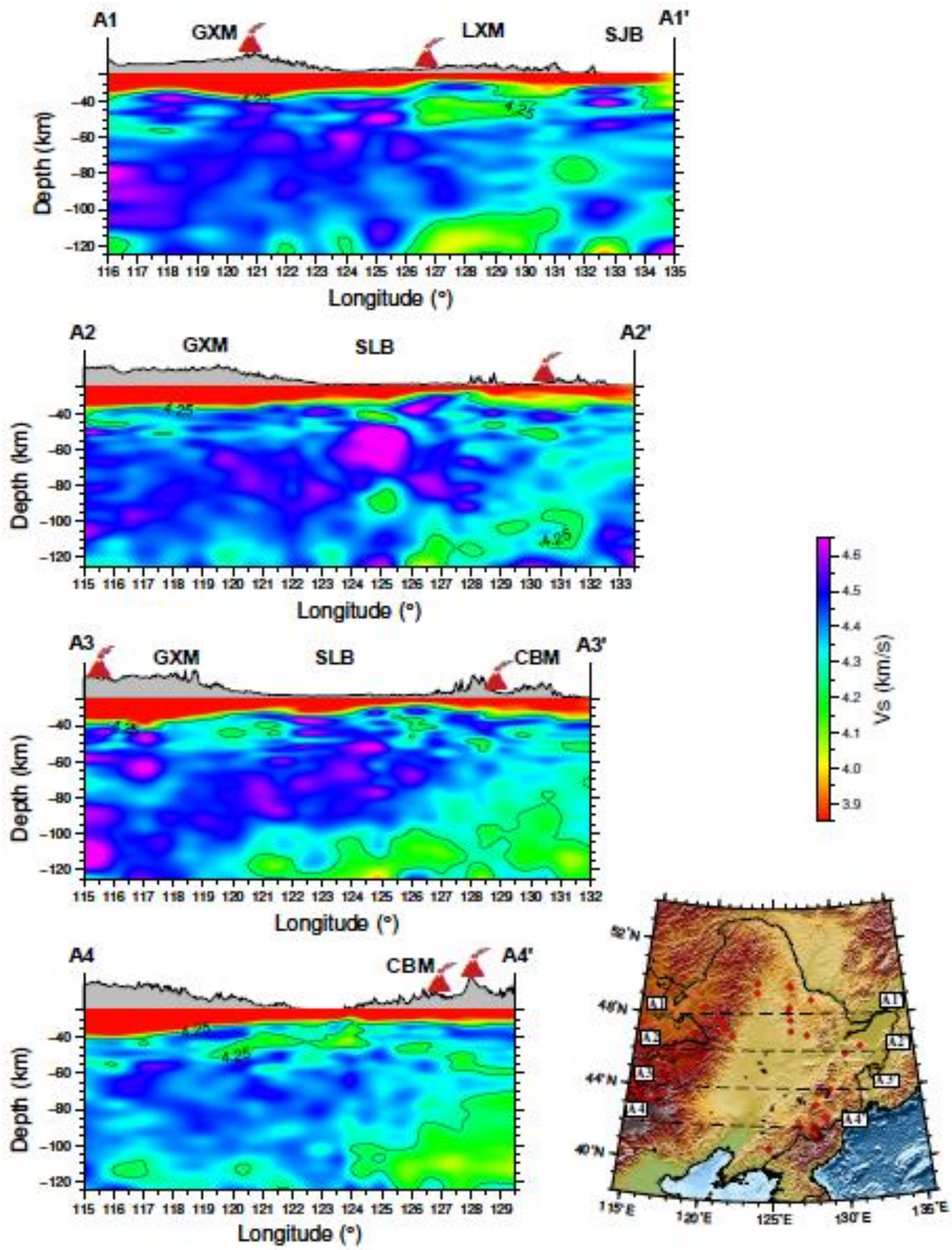

1073

1074 Figure 12. Vertical slices of S-wave velocity along profiles A1–A4 across the study area
1075 over the upper-mantle depths (25-125 km). CBM = Changbai mountains; GXM =
1076 Greater Xing'an mountain range; LXM = Lesser Xing'an mountain range; SJB =
1077 Sanjiang basin; SLB = Songliao basin.

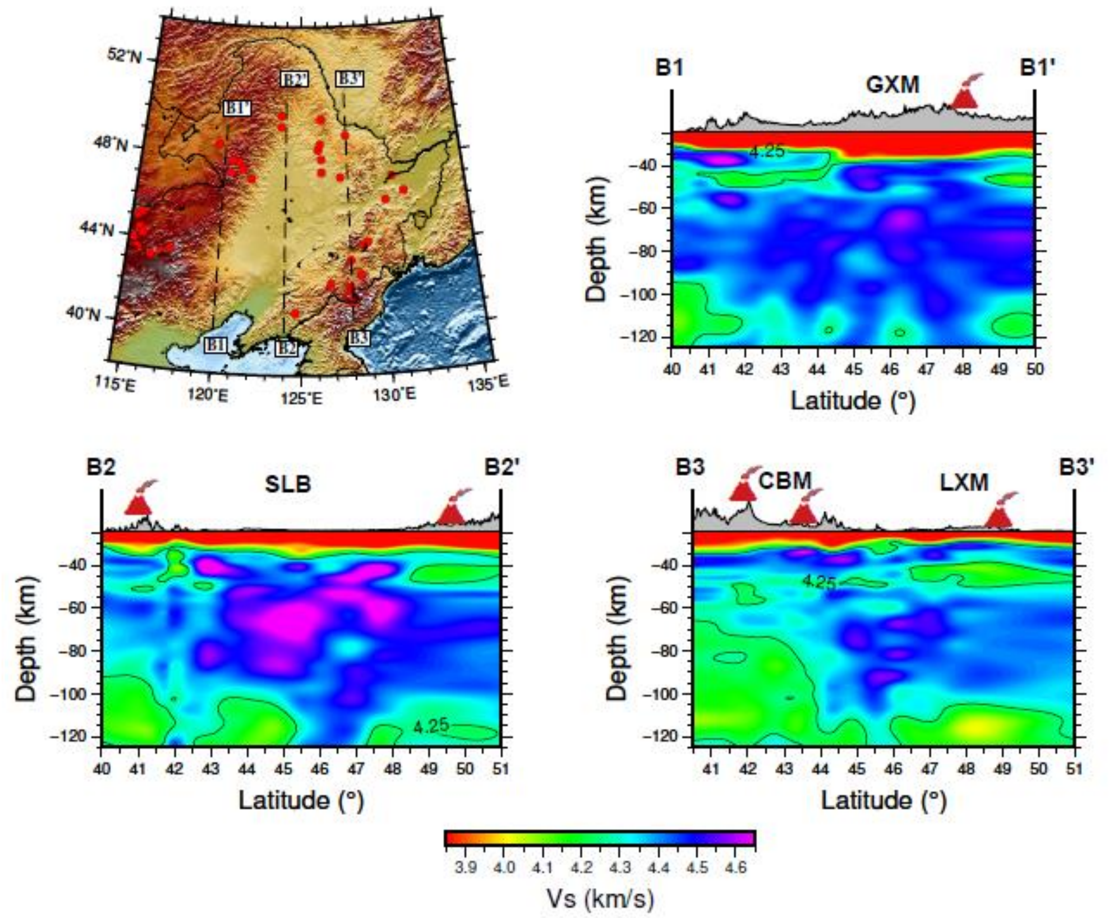

Figure 13. Vertical slices of shear-wave velocity along profiles B1–B3 across the study area over the upper mantle (25-125 km). CBM = Changbai mountains; GXM = Greater Xing'an mountain range; LXM = Lesser Xing'an mountain range; SLB = Songliao basin.

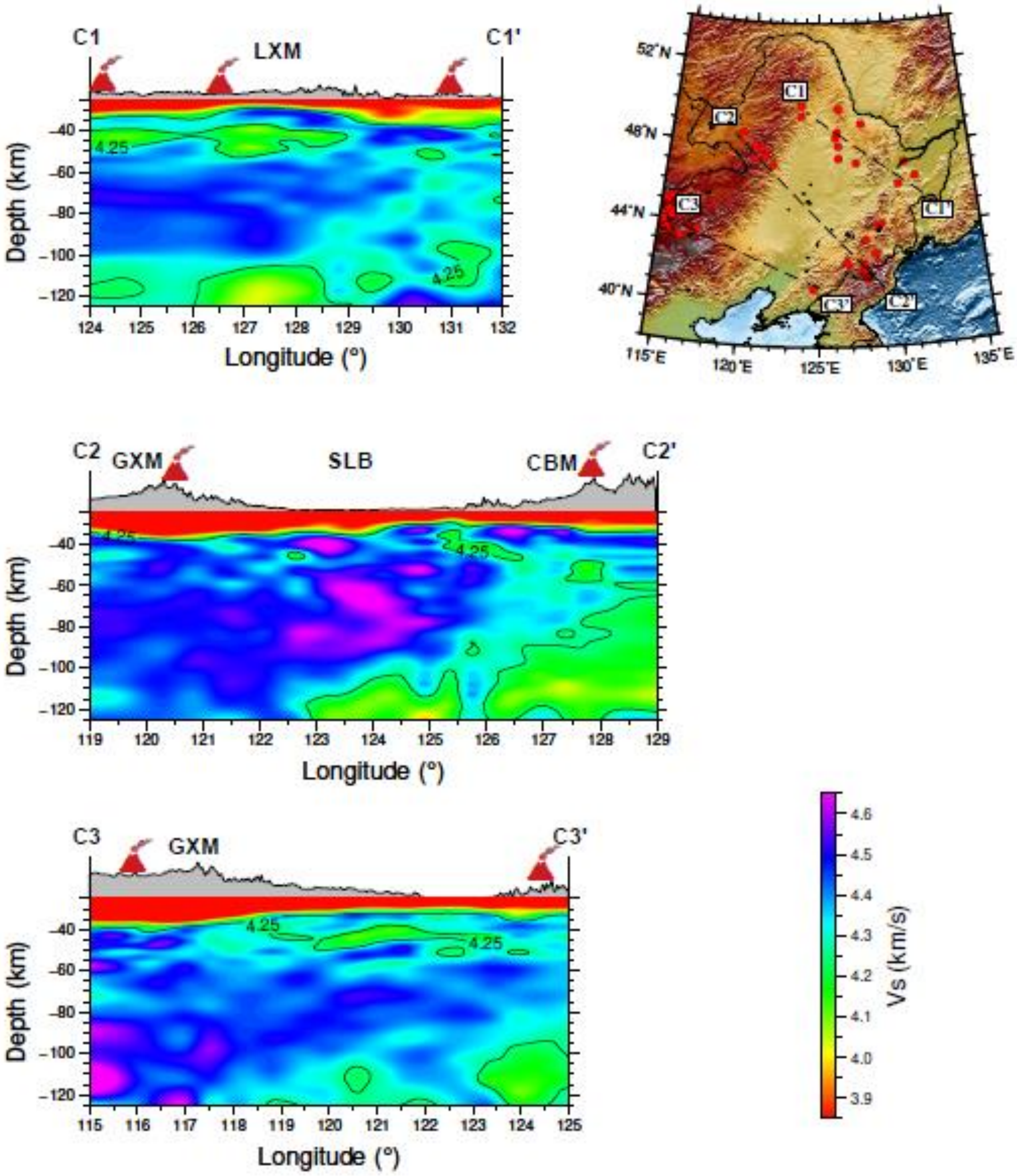

Figure 14. Vertical transects of S-wave velocity along profiles C1–C3 over the depth range of 25-125 km. CBM = Changbai mountains; GXM = Greater Xing'an mountain range; LXM = Lesser Xing'an mountain range; SLB = Songliao basin.

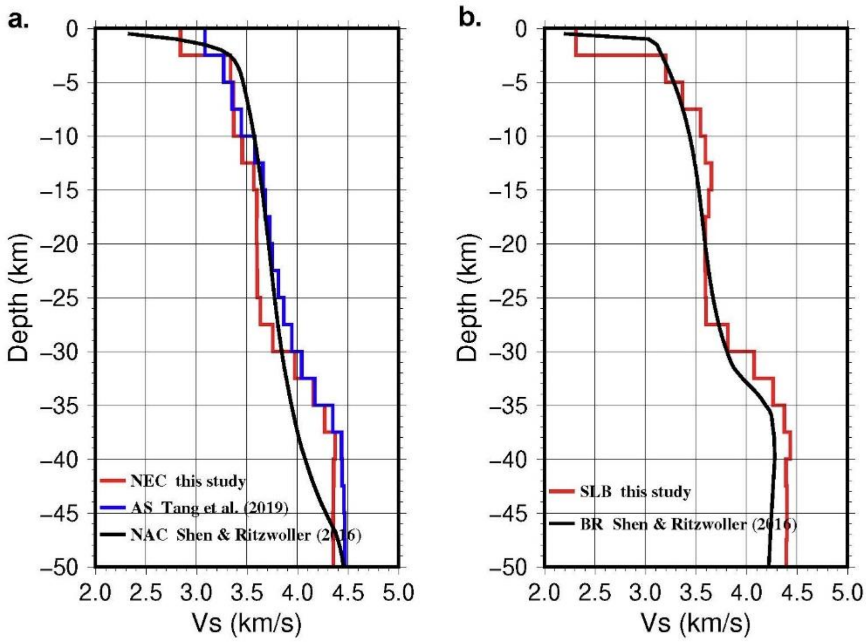

Figure 15. (a) 1-D average shear wave velocity structure beneath Northeast China (NEC, red line), the Arabian shield (AS, blue line, Tang et al., 2019), and the North American craton (NAC, black line, Shen & Ritzwoller, 2016). (b) 1-D average S-velocity model below the Songliao basin (SLB, red line) and the Basin and Range (BR, black line, Shen & Ritzwoller, 2016) in Western United States.

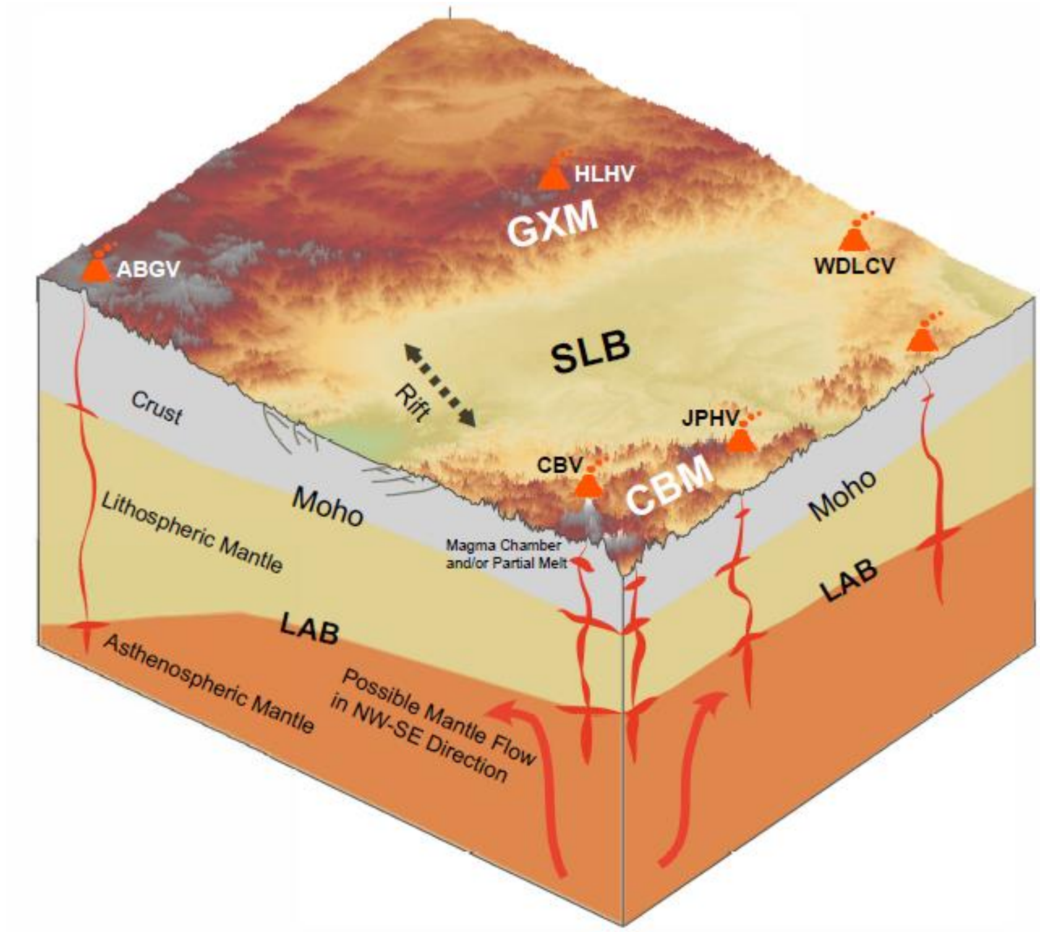

Figure 16. 3-D schematic diagram across the study area, showing the main structural features such as the lithospheric thickening westward, and the proposed Cenozoic volcanic/magmatic mechanism at lithospheric and sub-lithospheric levels below Northeast China. CBM = Changbai mountains; GXM = Greater Xing'an mountain range; SLB = Songliao basin; CBV = Changbaishan volcano; JPHV = Jingpohu volcano; WDLCV = Wudalianchi volcano; HLHV = Halaha volcano; ABGV = Abaga volcano; LAB = lithosphere-asthenosphere boundary.

Supporting Information for "Shear wave velocity structure beneath Northeast China from joint inversion of receiver functions and Rayleigh wave group velocities: Implications for intraplate volcanism"

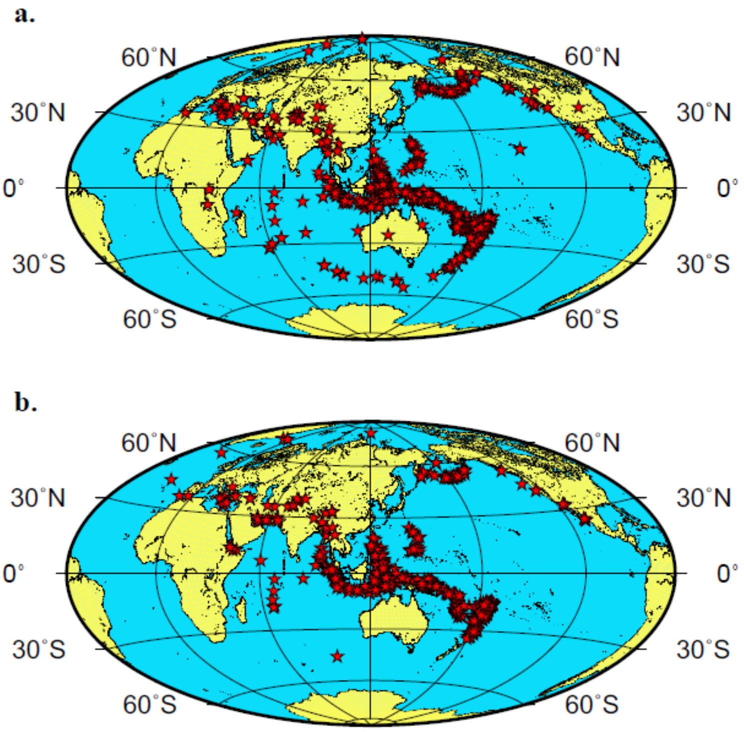

Figure S1. (a) Global distribution of earthquakes (2016–2019, red stars) for our receiver function analysis at the permanent CEA stations. (b) Global distribution of earthquakes (between 2009.09 and 2011.08, red stars) for obtaining receiver functions at the temporary NECESSArray sites.

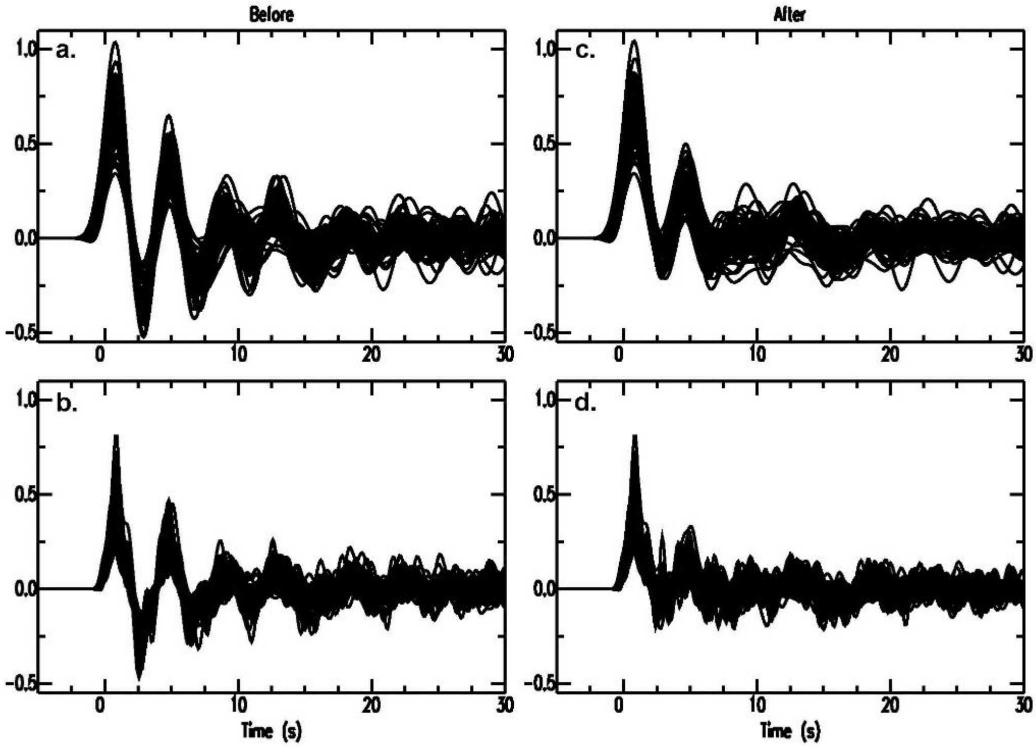

Figure S2. Radial receiver functions at low (fc ≤ 0.50 Hz, Gaussian width $\alpha = 1.0$) and high (fc ≤ 1.25 Hz, Gaussian width $\alpha = 2.5$) frequency bands recorded by station NEA7 (located in the SLB and marked in Figure 2) are plotted in panel a and b, respectively. Panel c and d exhibit the resulting receiver functions at the two frequency ranges after applying the resonance removal filter.

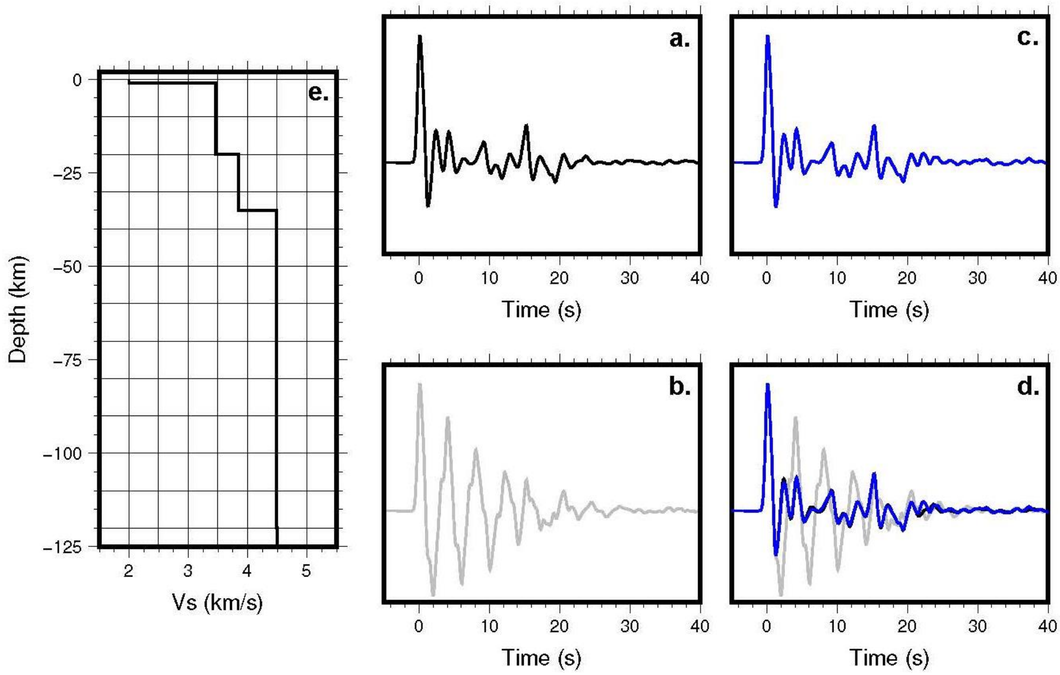

Figure S3. (a) Synthetic receiver function (ray-parameter 0.05 s/km, at Gaussian width of α = 2.5) corresponding to the true model in panel (e). Note that a 1.0 km thick sedimentary layer is presumed and the primary P-to-S phases triggered by the sedimentary structure are likely between 1 and 3 s. However, it does not account for the complex situation that energy reverberating within the sedimentary layer (i.e., multiples of converted shear waves). (b) Synthetic receiver function corresponding to the same true model, but including strong near-surface reverberations of converted shear phases. It is defined by the equation (2) in Yu et al. (2015). (c) Resulting receiver function after applying the resonance removal filter on the time series in panel (b). (d) Comparison between the synthetic receiver function without near-surface reverberations (black), the synthetic receiver function with strong near-surface multiples (gray), and the resulting receiver function after applying the resonance removal filter (blue). The blue trace is quite consistent with the black one (in both amplitude and lag time), which illustrates that the resonance removal filter effectively removes the near-surface multiples of converted shear phases and successfully recovers the right signals from deep interfaces.

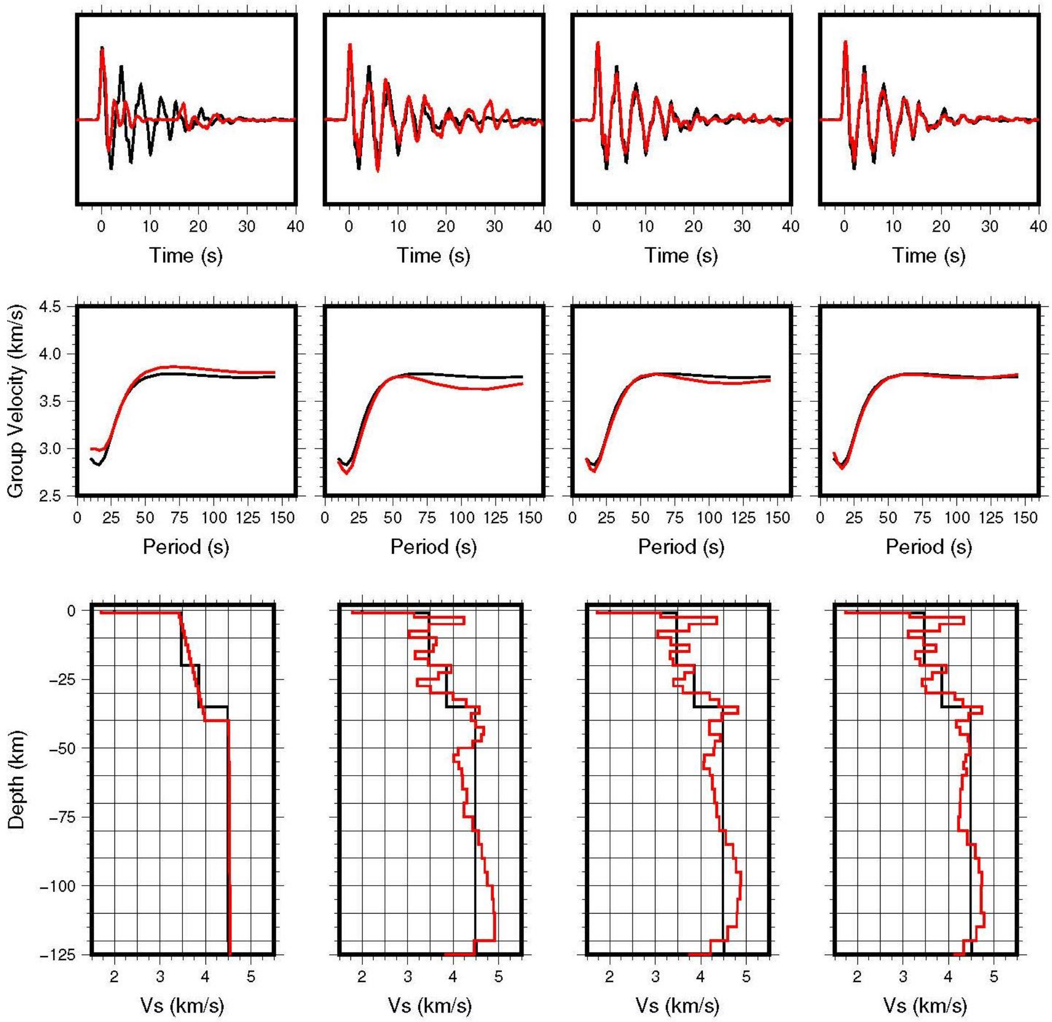

Figure S4. A synthetic test for joint inversion. Theoretical receiver function with strong near-surface reverberations (the one in Figure S3b) and Rayleigh wave group velocity dispersion curve that are corresponding to the true model (black) are represented by black lines. Evolution of the iterated solutions and the corresponding predicted data are shown by red lines. Note that the joint inversion converges to a solution, which however contains many artifacts and unsuccessfully recovers the true model.

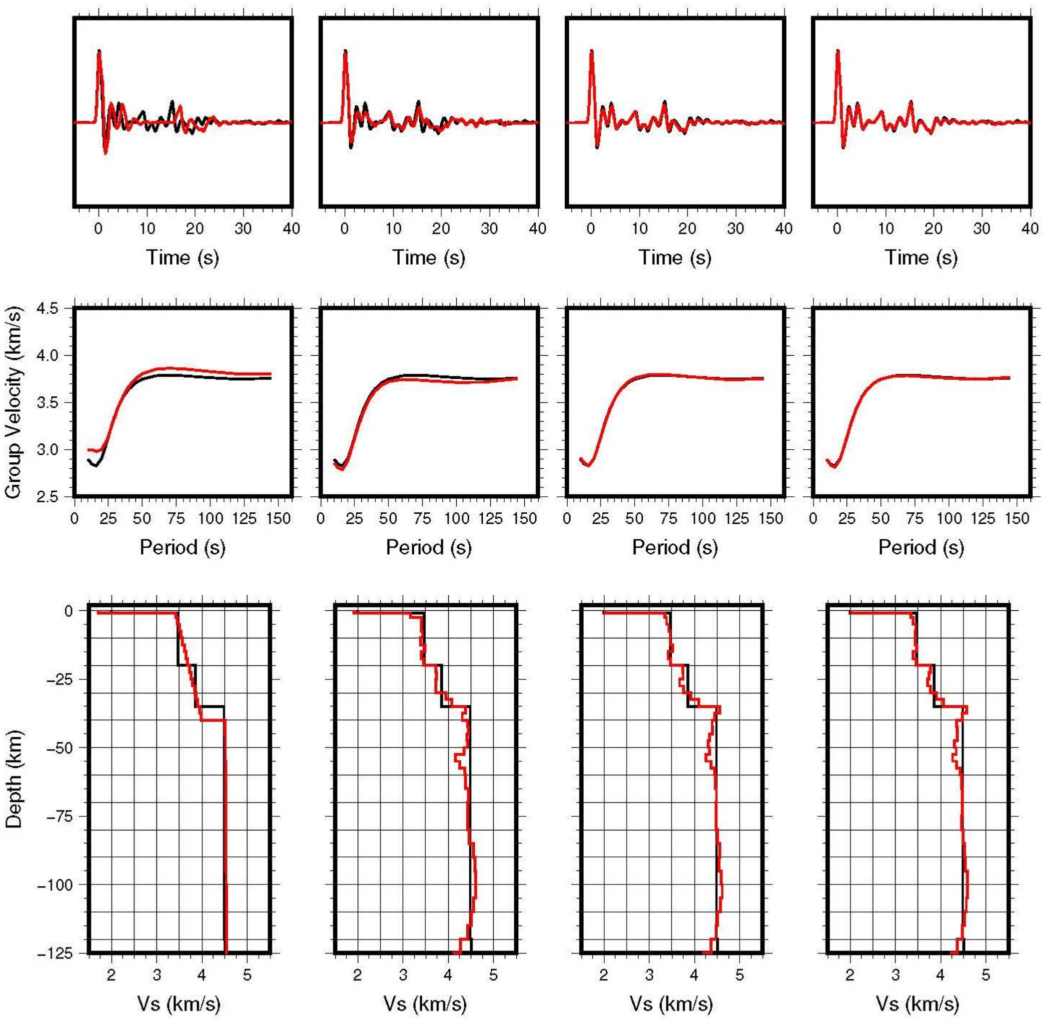

Figure S5. The resulting receiver function after the application of the resonance removal filter (the one in Figure S3c) is inverted jointly with synthetic Rayleigh wave dispersion data (black). Evolution of the iterated solutions and the predicted data are displayed by red lines. The inversion recovers the true model in three iterations.

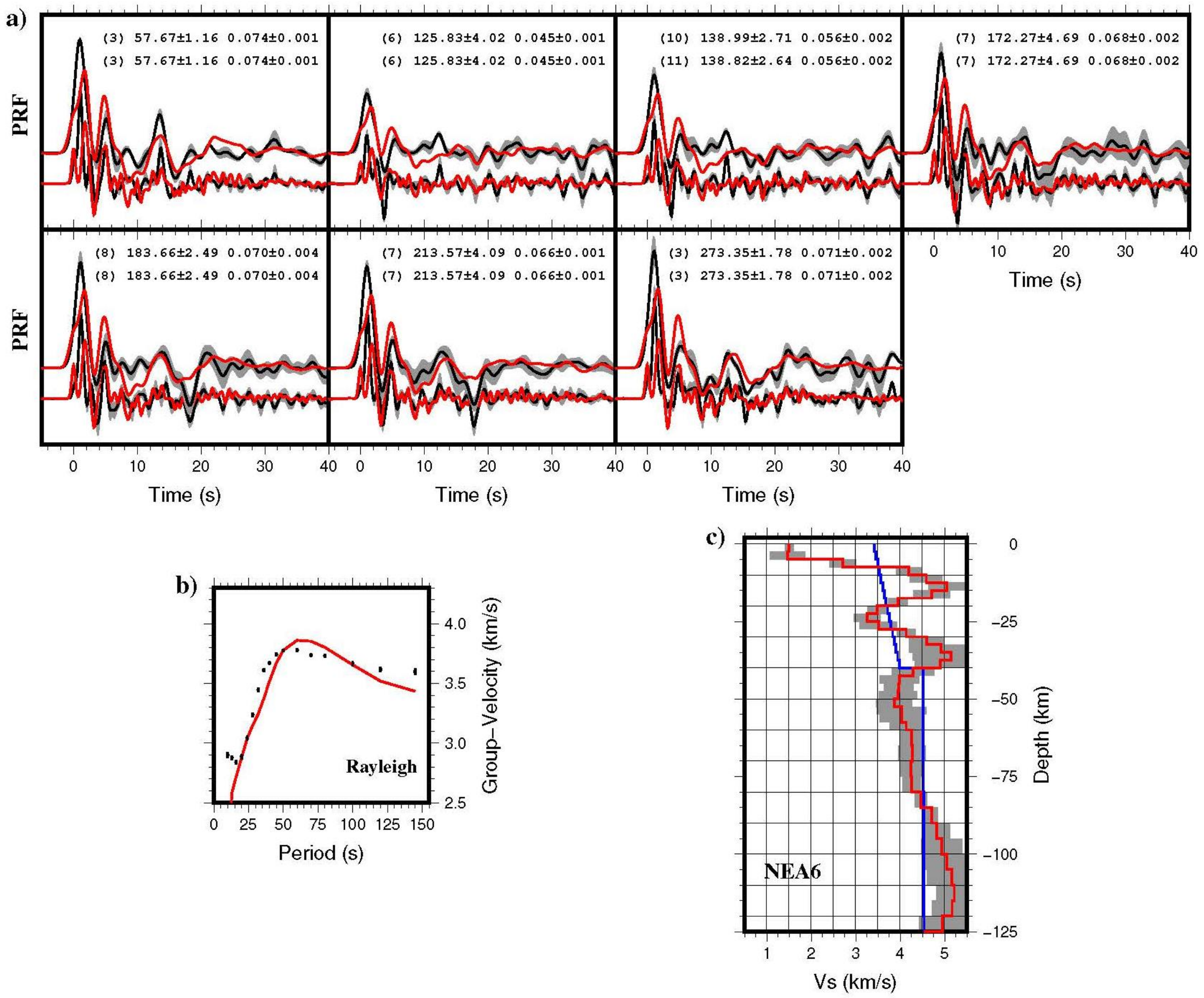

Figure S6. Unsuccessful joint inversion at station NEA6. The initial model (blue in panel c) that does not include a sedimentary layer is employed. Note that the solution (red in panel c) driven away from the convergence and the poor data fitting in both receiver functions (panels a) and Rayleigh wave dispersion velocities (panel b).

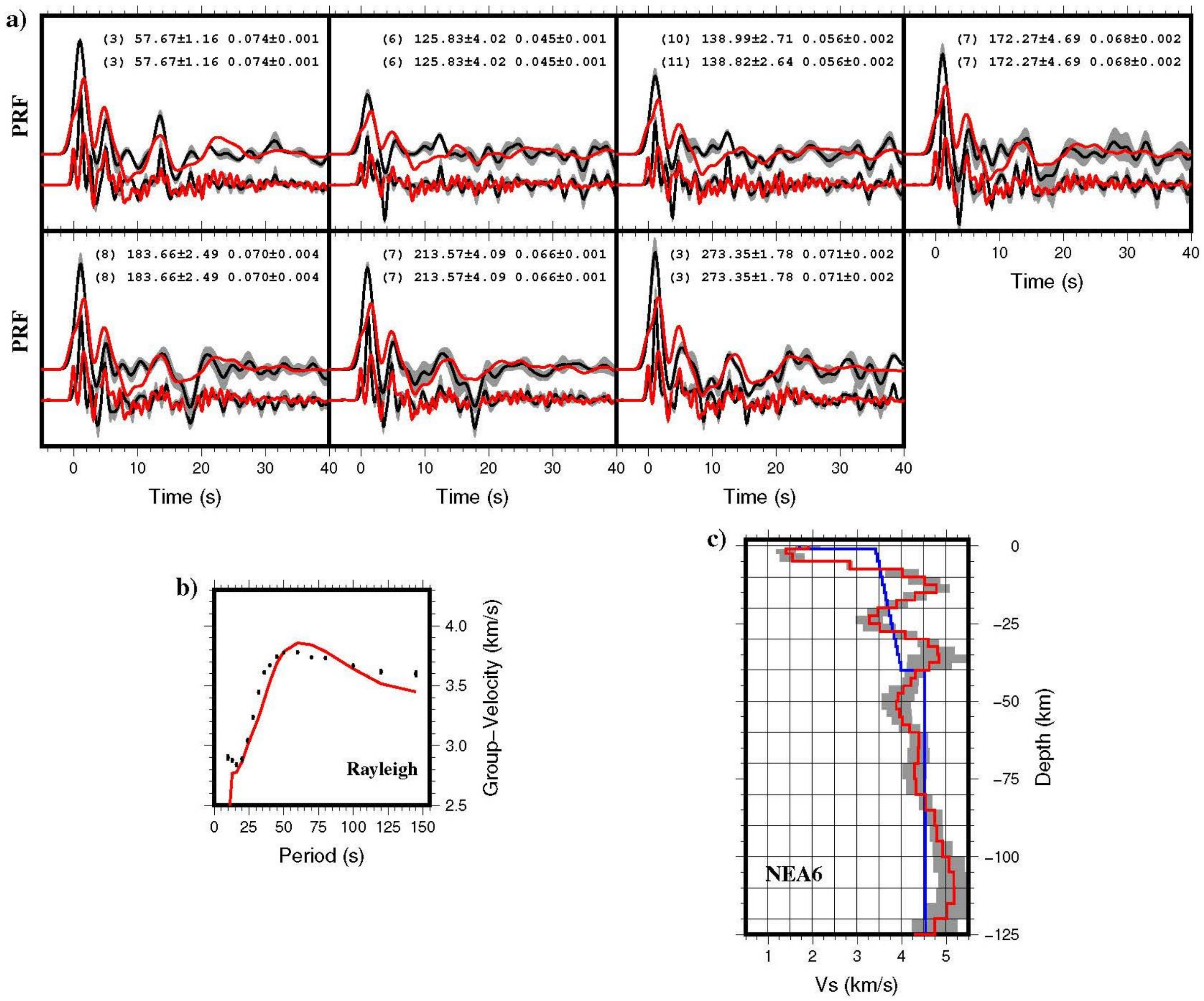

Figure S7. Joint inversion at NEA6, but applying a starting model with a 1.0 km thick sedimentary layer (blue in panel c). The inversion is still unsuccessful.

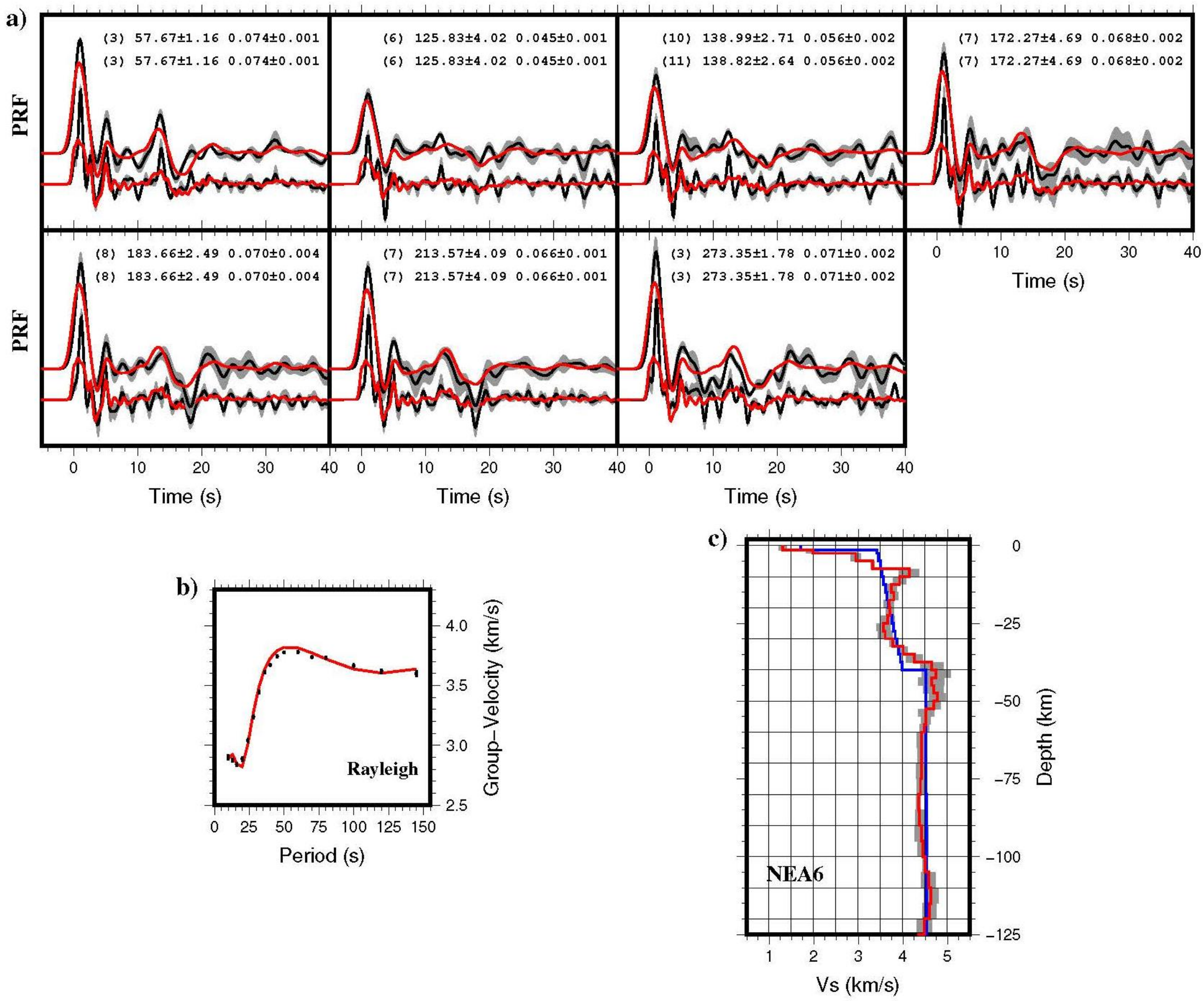

Figure S8. Joint inversion at NEA6, but employing an initial model with a 1.5 km thick sedimentary layer (blue in panel c). This case is successful. The inverted S velocity model is displayed in panel c. Note that the excellent match between predicted and observed data in both receiver functions (panels a) and dispersion curve (panel b).

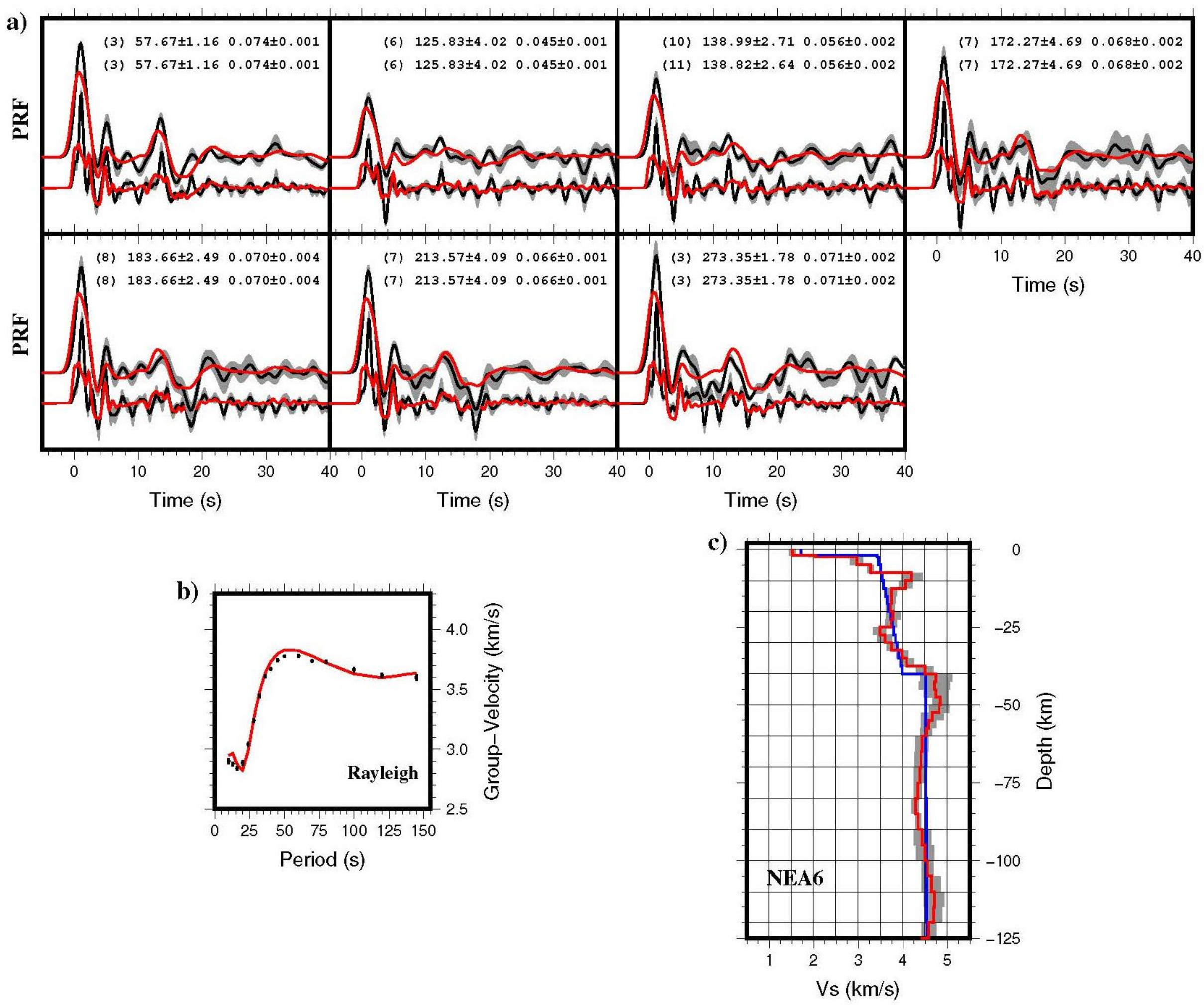

Figure S9. Joint inversion at NEA6, with a 2.0 km thick sedimentary layer in the initial model (blue in panel c).

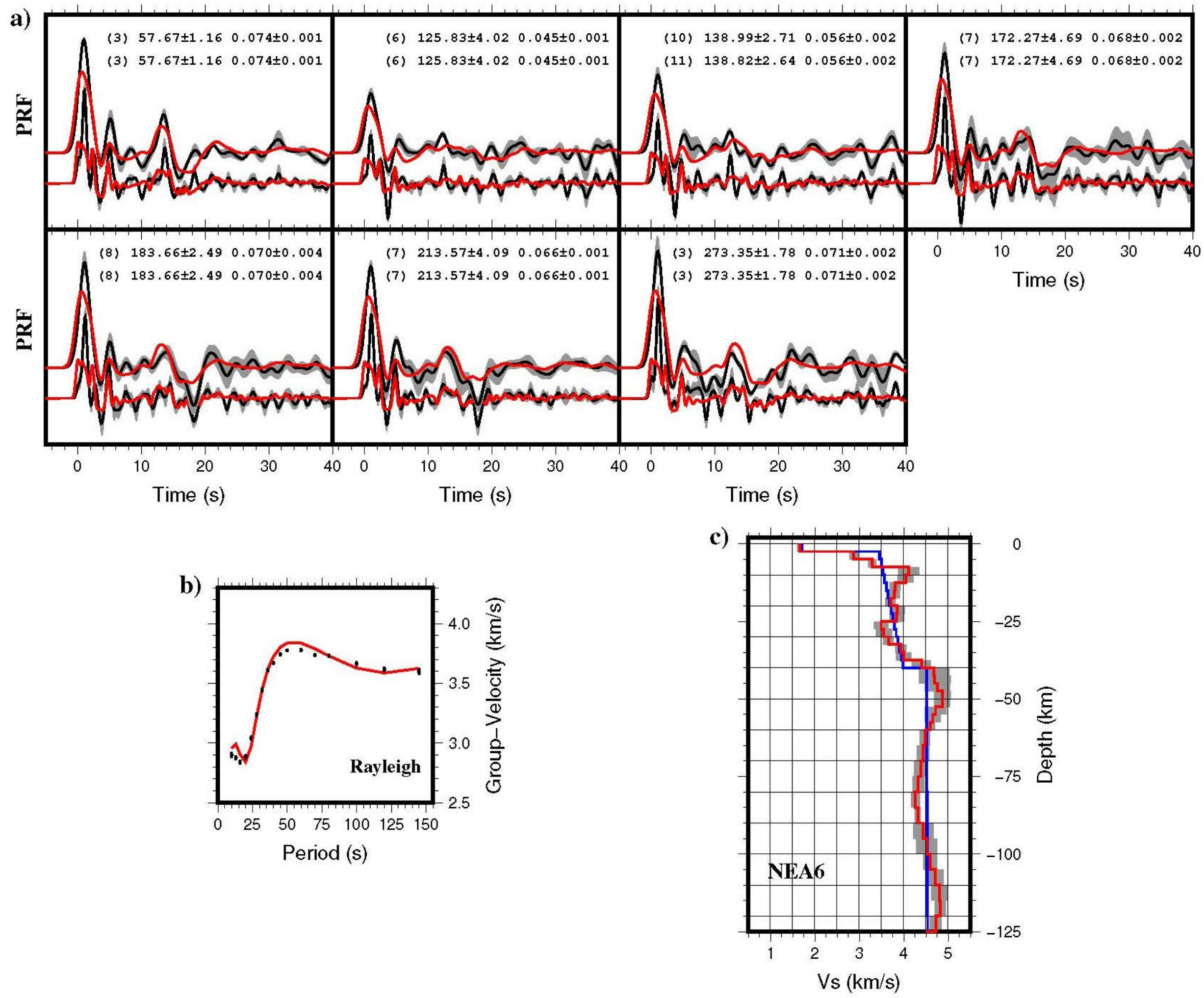

Figure S10. Joint inversion at NEA6, with a 2.5 km thick sedimentary layer in the starting model (blue in panel c).

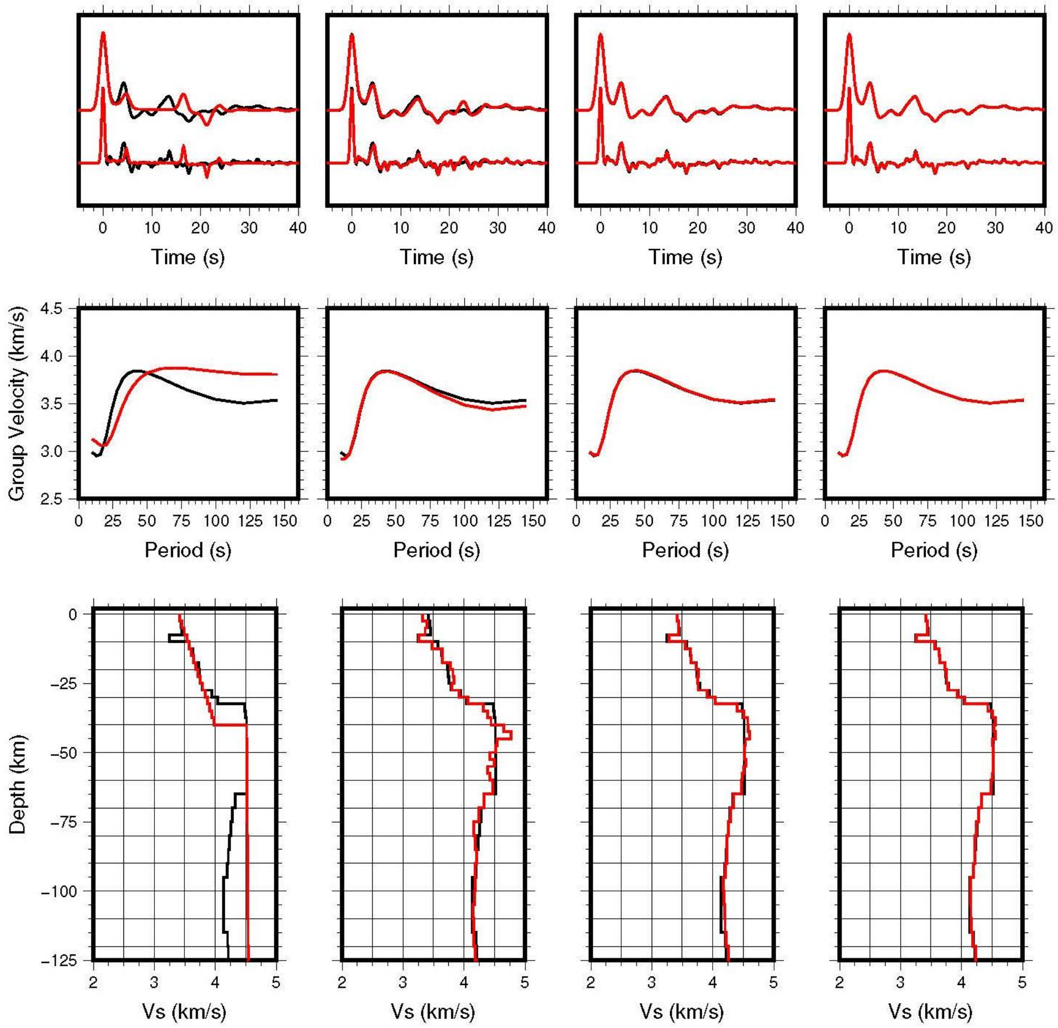

Figure S11. A synthetic joint inversion test. The true model (black) contains a 2.5 km thick low Vs anomaly in the crust and an upper-mantle low shear velocity zone below 65 km depth. The synthetic receiver functions (ray-parameter 0.05 s/km, at Gaussian widths of α = 2.5 and 1.0) and Rayleigh wave group velocity dispersion curve (at periods of 10–145 s) corresponding to the true model are represented by black lines. Evolution of the iterated solutions and the corresponding predicted data are shown by red lines. Note that the resulting model converged to the true solution and the presumed crustal and upper-mantle Vs anomalies are perfectly recovered in three iterations.

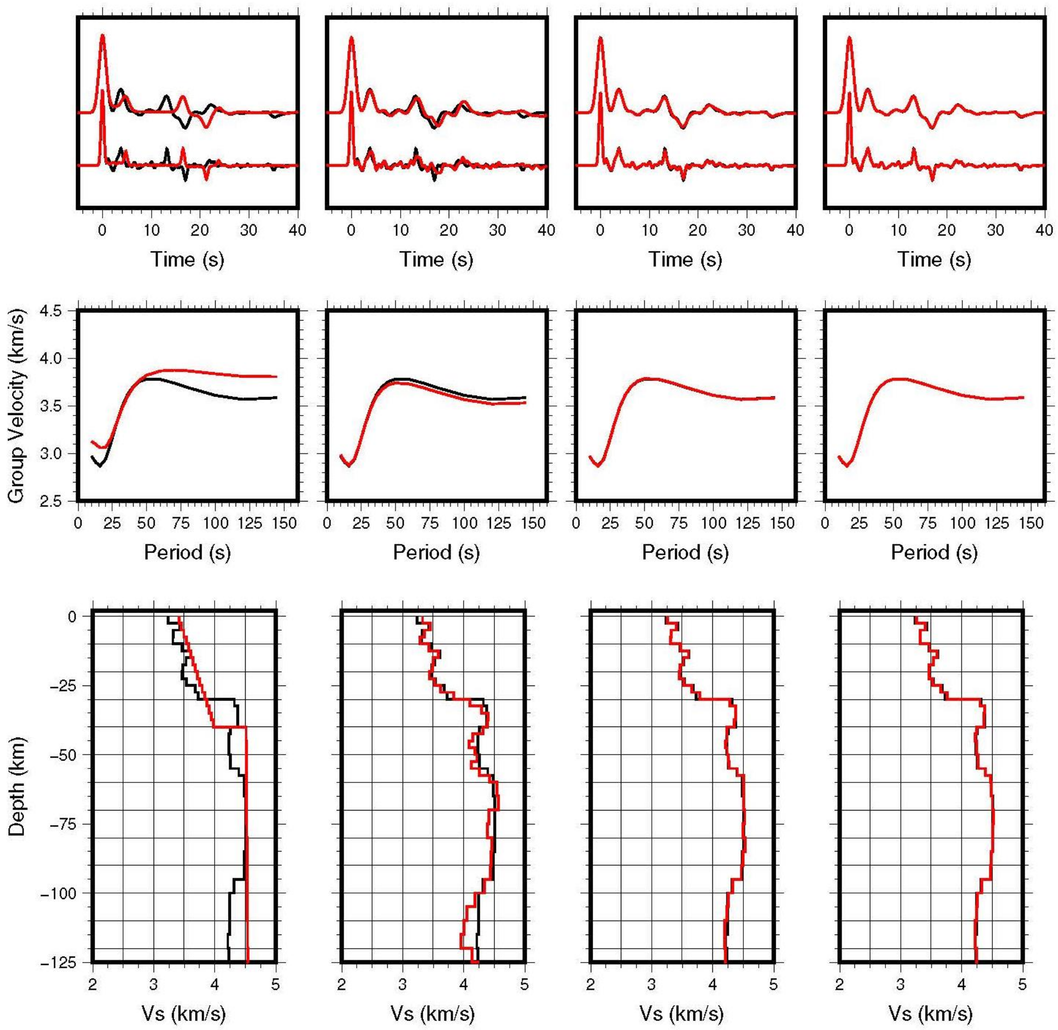

Figure S12. Same as Figure S11, but for a different true model. This true model (black) includes a slow S velocity feature at 40-60 km depths (i.e., uppermost-mantle levels) and an upper-mantle low velocity zone below 95 km. Note that the significant shear velocity anomalies at the crustal and upper-mantle depths are successfully recovered by joint inversion.